Numerical study of the impact of the channel shape on microchannel boiling heat transfer

M. Magnini[1*], O. K. Matar[2]

[1] *Department of Mechanical, Materials and Manufacturing Engineering, University of Nottingham, Nottingham NG7 2RD, United Kingdom*

[2] *Department of Chemical Engineering, Imperial College London, London SW7 2AZ, United Kingdom*

Abstract

Flow boiling in multi-microchannel evaporators is recognised as one of the most efficient cooling solutions for high-performance electronics, and has therefore received increasing attention during the recent years. Despite the extensive literature, there is no general agreement yet about the effect of the channel cross-sectional shape on the boiling heat transfer performance, which results on a limited availability of thermal design guidelines and tools. This article presents the results of a systematic analysis of the impact of the channel shape on the bubble dynamics and heat transfer, under flow boiling conditions. Simulations are carried out using a customised version of OpenFOAM, and the Volume-Of-Fluid method is chosen to capture the liquid-vapour interface dynamics. A benchmark flow model is utilised, where a single isolated bubble is seeded at the channel upstream and transported by a liquid flow across the diabatic section, which is heated by a constant and uniform heat flux. Flow conditions that apply well to the flow boil-

*Corresponding author. E-mail: mirco.magnini@nottingham.ac.uk

ing of water or refrigerant fluids in sub-millimetre channels at low heat flux ($\sim 10\,\mathrm{kW/m^2}$) are investigated, with cross-section width-to-height aspect-ratios ranging from 1 to 8, while the hydraulic diameter of the channel is fixed. This study emphasises that the heat transfer performances for different channel shapes are closely related to the perimetral distribution of the liquid film surrounding the very long bubbles. Square channels exhibit the highest heat transfer coefficients at low flow rates, due to a very thin liquid film that forms at the centre of the wall, but are more at risk of film dryout. High aspect-ratio rectangular channels may be beneficial at larger flow rates, as they promote the formation of an extended liquid film that covers up to 80 % of the cross-section perimeter. At larger aspect-ratios, the average heat transfer coefficient along the shorter wall becomes orders of magnitude smaller than the value detected along the longer wall, owing to a strong asymmetry in the liquid film perimetral distribution.
Keywords: Heat transfer, Boiling, Microchannel, Two-Phase, Non-circular channels, Thermal management

1. Introduction

Flow boiling in microchannel heat sinks is recognised as one of the most effective cooling solutions for high heat flux devices, with a wide variety of potential applications such as the thermal management of electronic components in computers [1], high energy physics particle detectors [2], and fuel cells [3], miniature refrigerating systems [4], cooling turbine blades, and battery packs cooling in hybrid vehicles [5], to name a few; the interested reader is referred to the reviews of Mudawar [5], Karayiannis and Mahmoud [6],

and Cheng and Xia [7], for a summary of the recent literature covering heat transfer, modelling, applications, and open issues. The heat transfer element is usually a multi-microchannel evaporator, i.e. a block made of highly-conductive material (e.g. copper, silicon) where several parallel microchannels are manufactured. In experimental flow boiling rigs, the evaporator is mounted with its bottom surface in direct contact with the heating element. In a cooling system driven by a pump, a fluid at saturated conditions (or slightly subcooled) enters the heat sink via the inlet manifold and leaves it as a mixture of liquid and vapour after flowing through the microchannels. Owing to the dissipation of the latent heat, flow boiling can effectively remove heat fluxes on the order of $\mathrm{MW/m^2}$ through heat exchange areas of a few $\mathrm{cm^2}$ [8].

Several different designs of the microchannels cross-sections have been proposed in the recent years, with the most traditional configurations being square and rectangular cross-sections. A schematic of the microchannel configuration of interest and the notation used in this work are introduced in Fig. 1. While there is general agreement that miniaturisation of the channels leads to better heat transfer, the impact of the cross-sectional shape is not yet fully-understood, because most of the independent studies tested a single microchannel design. Only a few authors attempted a systematic analysis of the channel shape; these are briefly reviewed below. To the best of our knowledge, Yen et al. [9] were the first to conduct a comparative study of square and circular microchannels, uniformly-heated, keeping a constant hydraulic diameter of $D_h = 0.2\,\mathrm{mm}$. The square channels exhibited larger heat transfer coefficients, in particular at higher heat flux and lower vapour quality, which

was attributed to a larger number of active nucleation sites at the corners of the square cross-section. Harirchian and Garimella [10, 11] performed the first systematic analysis of the channel aspect-ratio in noncircular shapes, employing the dielectric fluid Fluorinert FC77 and multichannel evaporators heated from the bottom. Harirchian and Garimella [10] tested seven channel geometries, with width $W = 0.1 - 5.85\,\text{mm}$ and constant height $H = 0.4\,\text{mm}$, thus spanning the range of aspect-ratios $\epsilon = W/H = 0.27 - 15.6$, and diameters $D_h = 0.16 - 0.71\,\text{mm}$. Although no specific dependence on ϵ was observed, the heat transfer was slightly higher for channels of $\epsilon < 1$ (i.e. with $W < H$) and smaller size ($D_h < 0.4\,\text{mm}$), where convective boiling was assumed to be the governing heat transfer mechanism. In Harirchian and Garimella [11], the authors tested the same range of aspect-ratios, with hydraulic diameters down to $D_h = 0.1\,\text{mm}$; they concluded that the cross-sectional area, and not the aspect-ratio, was the determinant geometric factor affecting boiling heat transfer, with the heat transfer coefficient increasing as the area (but also D_h) decreased. Soupremanien et al. [12] performed boiling experiments using the fluid Forane 365HX within single channels of $D_h = 1.4\,\text{mm}$, and $\epsilon = 2.3$ and 7, heated from below. The flatter channel yielded higher heat transfer coefficients at heat fluxes $q \leq 38\,\text{kW/m}^2$, while performances were similar at larger heat fluxes. Wang and Sefiane [13] carried out experiments using fluid FC72 in single, uniformly-heated, high aspect-ratio channels, $\epsilon = 10$ and 20, with different hydraulic diameters $D_h = 0.57 - 1.45\,\text{mm}$. They observed larger critical heat flux when $\epsilon = 10$, but this may be attributed to the larger channel height, which promoted the existence of a thicker liquid film between the bubble and the wall,

thus delaying film dryout. Fu et al. [14] performed a systematic analysis for $\epsilon = 0.17 - 1.2$ and constant $D_h = 1.12\,\text{mm}$, using the coolant HFE7100 in an evaporator with diverging channels, heated from below. The best heat transfer was achieved with the square channel, while performances deteriorated when $\epsilon < 1$. The authors ascribed this to the thinning of the liquid film along the shorter side of the channel (the width) as ϵ decreased, and to the consequent dryout, by referring to the earlier observations of Choi et al. [15] for the isothermal flow of trains of bubbles. However, the work of Choi et al. [15] was based on qualitative single-side bubble visualisation and there was no actual film thickness measurement; furthermore, as ϵ was decreased below unity, the channel height and therefore its hydraulic diameter reduced as well, thus not allowing the authors to discriminate between channel size and shape effects. Markal et al. [16] studied evaporators with microchannels of fixed size, $D_h = 0.1\,\text{mm}$ and $\epsilon = 0.37 - 5$, heated from below, using deionised water as a coolant. The heat transfer coefficient increased monotonically with ϵ, although differences were minimal when $\epsilon \geq 3.5$. Finally, a monotonic increase of the heat transfer coefficient with the aspect-ratio was also reported in the experimental work of Al-Zaidi et al. [17], who utilised single microchannels of $\epsilon = 0.5 - 2$ heated from below, a fixed $D_h = 0.46\,\text{mm}$, with the fluid HFE7100. The authors attributed the better heat transfer to the existence of an extended thin liquid film region between the bubble and the wider wall (the width), which enhanced heat transfer when the wider wall was facing the hot surface.

As summarised above, there is still substantial disagreement about the impact of the channel aspect-ratio, and each of the possible configurations,

characterised by $\epsilon < 1$, $\epsilon = 1$, and $\epsilon > 1$, were deemed as the best in at least one study. Furthermore, these studies disregarded completely, or simply speculated, about the impact of the channel shape on the topology of the thin film trapped between the liquid-vapour interface and the channel wall, which has been proven to have a considerable influence on the local heat transfer [18, 19, 20, 21].

Nonetheless, the topology of the liquid film around long bubbles propagating in isothermal flow conditions within noncircular channels has been studied extensively as a model for enhanced oil recovery, flow in porous media [22], drug delivery in pulmunary aiways [23], and capillary cleaning [24]. The early work of Wong et al. [25] provides quantitative parameters characterising the bubble shape on the cross-section at quasi-static conditions, based on asymptotic theory. Hazel and Heil [26] performed numerical simulations for finite values of the bubble capillary number (ratio of viscous to surface tension forces) and negligible Reynolds number (ratio of inertial to viscous forces). The bubble capillary number was defined as $\mathrm{Ca_b} = \mu_l U_{b,N}/\sigma$, with μ_l being the liquid dynamic viscosity, $U_{b,N}$ the speed of the bubble nose, and σ the surface tension; the bubble Reynolds number was defined as $\mathrm{Re_b} = \rho_l U_{b,N} D_h/\mu_l$, with ρ_l being the liquid density. They observed that above a threshold value of the capillary number, the cross-sectional bubble profile became axisymmetric, but no axisymmetric profile could be attained when $\epsilon > 2.04$. de Lózar et al. [27] performed experiments of isothermal bubble propagation in rectangular microchannels, with $\epsilon = 1 - 15$, and observed that the wet fraction (fraction of the cross-sectional area occupied by liquid) decreased with increasing ϵ when $\mathrm{Ca_b} < 10^{-3}$, whereas it increased when in-

creasing ϵ for $\mathrm{Ca_b} > 10^{-2}$. This means that the liquid film occupied a smaller cross-sectional area as ϵ was increased at low flow rates, while it covered a larger area as ϵ was increased at higher flow rates. de Lózar et al. [28] performed a numerical study under similar conditions and reported that, when $\mathrm{Ca_b} > 10^{-2}$, the bubble width (rescaled by the channel width) decreased as ϵ was increased, i.e. the liquid film left on the shorter wall was thicker in rectangular channels. Also, they found that the flow became approximately two-dimensional for tubes of $\epsilon \geq 8$, with the dynamics of the propagating front of the bubble converging towards that of a Saffman-Taylor finger instability.

The objective of the present work is to build upon the existing studies on isothermal bubbles, to perform a fundamental analysis of the role of the channel cross-section on the bubble dynamics and heat transfer, under flow boiling conditions. We conducted interface-resolving numerical simulations with an augmented version of the Volume-Of-Fluid (VOF) [29] method in OpenFOAM, which implements a phase-change model based on the Hertz-Knudsen-Schrage relationship [30]. We utilise an idealised flow model, where a single isolated bubble is seeded at the channel upstream and transported by a liquid flow across the diabatic section, which is heated by a constant and uniform heat flux. The bubble grows owing to the evaporation of the surrounding liquid and the resulting impact on heat transfer is via a convective boiling mechanism. We investigate a range of flow conditions that apply well to the flow boiling of water or refrigerant fluids in sub-millimetre channels at low heat flux ($q \sim 10\,\mathrm{kW/m^2}$), and study cross-sectional aspect-ratios of $\epsilon = 1 - 8$, while keeping the hydraulic diameter constant.

The rest of this paper is organised as follows: in Section 2, the numerical framework is introduced; the results of validation tests are illustrated in Section 3; in Section 4, the results of the systematic analysis of the channel shape on bubble dynamics, liquid film distribution, and heat transfer, are presented; in Section 5, the results are discussed in relation to some of the trends observed in the experimental literature; conclusions are summarised in Section 6.

2. Numerical framework

2.1. Governing equations

The transport equations governing the flow of two immiscible phases, here liquid and vapour, are formulated according to the VOF method. The two phases are treated as a single mixture fluid with variable properties across the interface, and a volume fraction field α is defined to map the phases throughout the flow domain. In each computational cell of the domain, α identifies the fraction of the cell occupied by the primary phase, which corresponds to vapour in the present case. Therefore, the volume fraction takes values of 1 in the vapour, 0 in the liquid, and $0 < \alpha < 1$ in cells that are cut by the interface. By means of the volume fraction field, the properties of the mixture fluid can be computed as an average over the two phases, e.g. the density ρ:

$$\rho = \alpha\rho_v + (1 - \alpha)\rho_l \tag{1}$$

where the subscripts v and l denote vapour and liquid-specific properties, respectively.

The advantage of the single-fluid formulation is that a single set of conservation equations holds for both phases, which share a unique velocity, pressure and temperature field. We consider the incompressible and laminar flow of two Newtonian fluids that undergo phase-change, for which the governing equations of mass, momentum and energy are expressed as follows:

$$\nabla \cdot \boldsymbol{u} = \left(\frac{1}{\rho_v} - \frac{1}{\rho_l}\right)\dot{m}|\nabla\alpha| \tag{2}$$

$$\frac{\partial(\rho\boldsymbol{u})}{\partial t} + \nabla \cdot (\rho\boldsymbol{u}\boldsymbol{u}) = -\nabla p + \nabla \cdot \mu\left[(\nabla\boldsymbol{u}) + (\nabla\boldsymbol{u})^T\right] + \boldsymbol{F_\sigma} \tag{3}$$

$$\frac{\partial(\rho c_p T)}{\partial t} + \nabla \cdot (\rho c_p \boldsymbol{u} T) = \nabla \cdot (\lambda\nabla T) - \dot{m}[h_{lv} - (c_{p,v} - c_{p,l})T]|\nabla\alpha| \tag{4}$$

where $\boldsymbol{u}$ indicates the fluid velocity, $\dot{m}$ the mass flux due to phase-change (positive when from liquid to vapour), t the time, p the pressure, μ the dynamic viscosity, $\boldsymbol{F_\sigma}$ the surface tension force vector, T the temperature, c_p the constant pressure specific heat, λ the thermal conductivity, and h_{lv} is the latent heat of vaporisation. Under the conditions simulated, temperatures do not vary by more than a few degrees Kelvin and therefore all the fluid-specific properties (e.g. ρ_v, ρ_l, μ_v, μ_l, etc.) are considered constant in this work.

The surface tension force is formulated according to the Continuum Surface Force method [31] and computed as $\boldsymbol{F_\sigma} = \sigma\kappa|\nabla\alpha|$, where σ is the surface tension coefficient (considered constant) and κ the local interface curvature. The latter is estimated by means of derivatives of the volume fraction field, $\kappa = \nabla \cdot (\nabla\alpha/|\nabla\alpha|)$. The interface mass flux due to boiling $\dot{m}$ is estimated as a function of the local interface superheat according to the Hertz-Knudsen-Schrage relationship [32], and adopting the linearisation proposed by Tana-

sawa [33] for low values of the superheat:

$$\dot{m} = \frac{2\gamma}{2-\gamma}\left(\frac{M}{2\pi R_g}\right)^{1/2}\frac{\rho_v h_{lv}(T_{lv}-T_{sat})}{T_{sat}^{3/2}} \tag{5}$$

where γ is the evaporation coefficient (here set to 1 according to preliminary test benchmarks [34, 30]), M is the molecular weight of the fluid, R_g the universal gas constant, and T_{lv} the temperature at the liquid-vapour interface.

The mathematical problem is closed by a transport equation for the volume fraction, which allows the numerical model to update the location of the interface, and therefore the mixture fluid properties, as the two-phase flow evolves across the computational mesh:

$$\frac{\partial \alpha}{\partial t} + \nabla \cdot (\alpha \boldsymbol{u}) = \frac{1}{\rho_v}\dot{m}|\nabla \alpha| \tag{6}$$

The source terms related to phase-change appearing at the right-hand sides of Eqs. (2), (4), and (6), are smoothed across the interface to avoid numerical instabilities, as originally proposed by Hardt and Wondra [35]. Details of the procedure for the solver utilised in this work are included in Ferrari et al. [30].

2.2. Discretisation methods

The equations presented in the previous section are solved using a customised version of OpenFOAM's VOF-based solver InterFoam (solver for two immiscible incompressible phases in an isothermal flow), modified to include the energy equation and the phase-change model as described above [30]. The transport equations are discretised with a finite-volume method on a collocated grid arrangement. The volume fraction Eq. (6) is discretised with a first-order time-explicit scheme based on the MULES (Multidimensional

Universal Limiter for Explicit Solution) algorithm [36], whereas the remaining equations are integrated in time with a first-order implicit scheme. The divergence operators are discretised using second-order TVD (Total Variation Diminishing) schemes [37], whereas Laplacian operators are discretised with central finite-differences. The PISO (Pressure Implicit Splitting of Operators) algorithm [38] is utilised to iteratively update pressures and velocities (3 corrections set) within each time-step. The residuals thresholds for the iterative solution of the flow equations are set to 10^{-6} for the velocity, 10^{-8} for the pressure, and 10^{-10} for the temperature. The time-step of the simulation is variable and is calculated based on a maximum allowed Courant number of 0.5.

3. Validation

3.1. Adiabatic bubble dynamics

The heat transfer induced by the flow of long confined bubbles within microchannels is strongly dependent on the thickness of the liquid film trapped between the liquid-vapour interface and the channel wall, as it was first suggested by the theoretical model of Thome et al. [18], and later on confirmed by the experiments of Rao and Peles [20] and Han et al. [21], and the numerical simulations of Magnini and Thome [19].

The topology of the liquid film surrounding long gas bubbles propagating in square and rectangular channels is substantially different from that observed in circular channels, see the schematic in Fig. 1. We consider a long bubble travelling with speed $U_{b,N}$ across a microchannel of width W and height H, $W \geq H$. The hydraulic diameter of the channel is $D_h = 4A/P$,

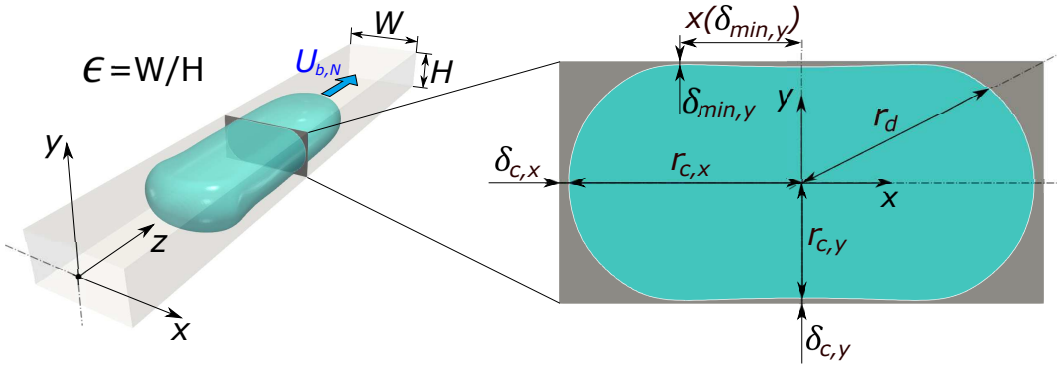

Figure 1: Flow configuration under analysis and notation used in this work. An elongated bubble travels at a speed $U_{b,N}$ across a microchannel of width W and height H, $W \geq H$. The bubble traps a thin film of liquid against the channel wall. The thickness of the film measured at the centre of the top wall ($x = 0$), along the vertical direction, is $\delta_{c,y}$ (vertical bubble radius: $r_{c,y} = H/2 - \delta_{c,y}$); the thickness measured at the centre of the side wall ($y = 0$), along the horizontal direction, is $\delta_{c,x}$ (horizontal bubble radius: $r_{c,x} = W/2 - \delta_{c,x}$). When the film profile along the top wall changes concavity, a dimple forms on the interface profile; the minimum film thickness value detected in the correspondence of the dimple is denoted as $\delta_{min,y}$; its distance from the $y-$axis ($x = 0$) is indicated as $x(\delta_{min,y})$.

with $A = HW$ being the channel area and $P = 2(H + W)$ its perimeter; the aspect-ratio of the channel is $\epsilon = W/H$, with $\epsilon \geq 1$. In order to describe the flow, we adopt a Cartesian reference frame centred at the channel longitudinal axis, where z identifies the streamwise coordinate, y denotes the vertical coordinate and x the horizontal one. Gravitational forces are neglected, and hence we assume that the flow on the transversal $x - y$ plane has $\pi/2$ symmetry. Surface tension forces tend to squeeze the liquid film against the walls, thus making the liquid film along the walls thinner, whereas thicker films are established at the corners [25]. We define as $\delta_{c,x}$ and $\delta_{c,y}$ the

film thicknesses measured in the horizontal ($y = 0$) and vertical symmetry planes ($x = 0$), respectively, with $r_{c,x}$ and $r_{c,y}$ being the respective bubble radii ($r_{c,x} + \delta_{c,x} = W/2$ and $r_{c,y} + \delta_{c,y} = H/2$). The perimetral distribution and thickness of the liquid film depend on the ratio of viscous to capillary forces, quantified by the bubble capillary number $\mathrm{Ca_b} = \mu_l U_{b,N}/\sigma$, on the ratio of inertial to viscous forces, identified by the bubble Reynolds number, $\mathrm{Re_b} = \rho_l U_{b,N} D_h/\mu_l$, and on the aspect-ratio of the cross-section [27]. For decreasing values of $\mathrm{Ca_b}$, or increasing values of ϵ, the bubble interface develops a reversed concavity along the channel walls [25]. This appears first along the longer wall (here the top wall, see Fig. 1), while further smaller capillary numbers are necessary in order for the interface curvature to change sign along the shorter wall. This change of concavity causes a dimple on the bubble interface, where a locally minimum value of the film thickness is detected. In the range of $\mathrm{Ca_b}$ studied in this work, the interface curvature changes sign only along the top wall, as sketched in Fig. 1, where a minimum film thickness value $\delta_{min,y}$ is identified. These features of the liquid-vapour interface are expected to have a significant impact on heat transfer, and hence it is imperative for the numerical solver to capture accurately the dynamics of the thin film as the bubble evolves in the microchannel.

In order to benchmark the solver, we have performed simulations of the adiabatic flow of long bubbles within a square channel ($\epsilon = 1$), and compared the results with the numerical study of Hazel and Heil [26] and de Lózar et al. [28], which were obtained with a high-accuracy solver based on the finite-element solution of the Stokes flow equations ($\mathrm{Re_b} \ll 1$), discretised on an interface-fitted mesh. We consider a square microchannel where a

fully-developed laminar flow of liquid is imposed at the inlet, together with a zero-gradient condition for the pressure; at the walls, a no-slip condition is applied; at the outlet, the pressure is fixed to zero and the velocity is given a zero-gradient condition. Owing to the $\pi/2$ symmetry of the flow, only one quarter of the cross-section is simulated, while symmetry boundary conditions are utilised on the $x = 0$ and $y = 0$ planes. A long gas bubble is initialised close to the channel inlet and it is pushed downstream by the liquid flow; when the bubble shape and speed reach a steady-state condition, the simulation is terminated. The liquid to gas density and viscosity ratios are respectively fixed to 1000 and 100. These ratios ensure that the results are independent of the bubble density and viscosity, as indicated by the numerical study of Kang et al. [39]. In Stokes flow conditions, the bubble dynamics is fully-determined by the values of the capillary number alone, here varied within the range $\mathrm{Ca_b} = 0.002 - 1$. At low capillary numbers, the liquid film thickness δ reaches values as small as $\delta = 0.01 R_h$, with R_h being the hydraulic radius of the channel ($R_h = D_h/2$). The accurate description of the flow in such thin liquid films is ensured by employing a near-wall refined computational mesh, with about 10 grid elements discretising the film, optimised upon a preliminary grid convergence study.

The results of the comparison with the numerical simulations of Hazel and Heil [26] and de Lózar et al. [28] are reported in Fig. 2. Figure 2(a) shows the radius of the bubble extracted at a distance of $11R_h$ behind the bubble tip, with r_c being the radius in the horizontal or vertical symmetry plane (subscripts x and y are dropped as $r_{c,x} = r_{c,y}$) and r_d the radius measured along the diagonal plane. As a general trend, the bubble radius

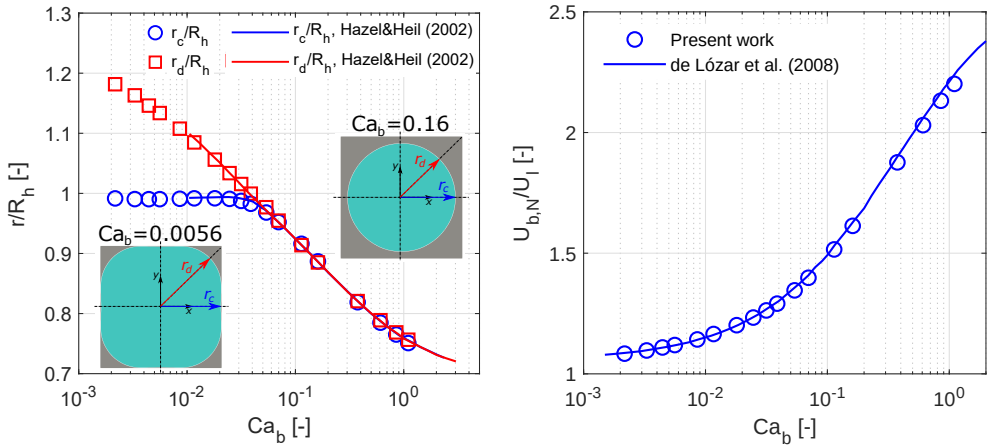

(a) (b)

Figure 2: Comparison with Hazel and Heil [26] and de Lózar et al. [28] numerical study of the isothermal propagation of long bubbles in a square channel ($\mathrm{Re_b} \ll 1$): (a) bubble radius at the centre of the channel wall, r_c, and along the diagonal, r_d, measured $11R_h$ behind the tip of the bubble nose; (b) bubble to average liquid velocity ratio. The insets in (a) depict the bubble profile on the cross-section for two selected values of $\mathrm{Ca_b}$.

increases monotonically as the capillary number is reduced, in agreement with Bretherton's traditional thin-film theory [40]. When $\mathrm{Ca_b} > 0.05$, $r_d = r_c$ and the bubble cross-section exhibits an axisymmetric profile, see the inset in Fig. 2(a). As $\mathrm{Ca_b}$ is decreased below 0.05, r_d and r_c diverge because the radius along the diagonal keeps increasing, whereas r_c is limited by the confinement effect of the channel walls, such that r_c reaches an approximately constant value of $r_c = 0.99R_h$. When $\mathrm{Ca_b} \leq 0.01$, the bubble profile along the wall changes concavity, thus forming a dimple where the local film thickness falls below δ_c. The results of our simulations agree very well with the data of Hazel and Heil [26], who investigated the range $\mathrm{Ca_b} = 0.01 - 10$. At the

lowest capillary number tested here, $\mathrm{Ca_b} = 0.002$, the bubble radius along the diagonal has reached the value of $r_d/R_h = 1.182$, which is very close to the value of 1.195 predicted by the asymptotic theory of Wong et al. [25] for $\mathrm{Ca_b} \to 0$.

Figure 2(b) plots the bubble speed, rescaled with the average liquid velocity U_l, as a function of the capillary number. The thicker film induced by increasing $\mathrm{Ca_b}$ results in a large bubble speed relative to the average liquid velocity. Note that the rescaled bubble speed is closely related to the void fraction of the two-phase flow, as the fraction of the cross-sectional area occupied by the vapour can be estimated as U_l/U_b [30]. Our results compare well with those of de Lózar et al. [28]; at the lowest $\mathrm{Ca_b}$ tested, $U_{b,N}/U_l = 1.084$, which is in good agreement with the value of 1.064 predicted by Wong et al. [25] for vanishing capillary numbers.

3.2. Boiling dynamics

The phase-change model utilised in this work was extensively validated in previous studies. Magnini et al. [34] and Ferrari et al. [30] simulated the heat-transfer-controlled growth of a vapour bubble in an infinite pool of superheated liquid. The authors compared the simulations results with the analytical solution for the time-dependent bubble radius provided by Scriven [41], and obtained excellent agreement. The same boiling module was employed by Magnini and Thome [42] to simulate slug flow boiling in a circular microchannel for a continuous train of bubbles. The time-averaged values of the heat transfer coefficient extracted from the simulations compared well with the experimental boiling heat transfer data of Consolini and Thome [43]. They compared also the velocity of the bubble nose, as it advanced and

accelerated within the channel, against different prediction methods from the literature, and reported a best match of trends and magnitudes with a theoretical model proposed by Consolini and Thome [44]. In the systematic analysis of the microchannel aspect-ratio developed below, further direct and indirect validations of the numerical model will be provided by comparing the results of the simulations with the available experimental data and theoretical models.

4. Results

4.1. Simulation setup

We consider microchannels of square and rectangular cross-section, of constant hydraulic diameter D_h. The channel is split into an initial adiabatic section of length $10D_h$, followed by a $20D_h$ long section heated with a constant heat flux q, uniformly distributed around the perimeter; a schematic of the flow configuration is provided in Fig. 3. The coordinate system is the same as that illustrated in Fig. 1. We neglect gravitational forces and assume that the flow has $\pi/2$ symmetry on the cross-section, so that only a quarter of the channel is simulated ($x \geq 0$ and $y \geq 0$). We investigate the range of cross-sectional aspect-ratios $\epsilon = W/H = 1 - 8$, where W and H can be arbitrarily interchanged due to the flow symmetry. We limit our study to $\epsilon \leq 8$ because the flow is expected to converge to a two-dimensional model for larger aspect-ratios [28]; this will be verified by the simulation results. Since the hydraulic diameter is constant, the channel width and height can be calculated as follows:

$$W = \frac{D_h}{2}(1+\epsilon), \quad H = \frac{D_h}{2}\frac{1+\epsilon}{\epsilon} \tag{7}$$

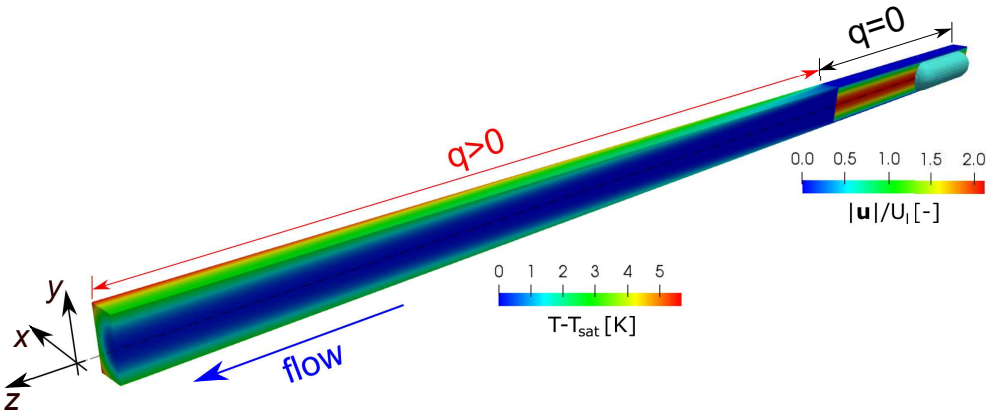

Figure 3: Initial flow configuration for flow boiling simulations (here shown for $\epsilon = 1$). Only half of the channel is showed, for visualisation purpose. An elongated vapour bubble (coloured in light blue) is patched at the upstream of the channel. The channel is split into an upstream adiabatic section of length $10D_h$ and a downstream diabatic section of length $20D_h$, heated with a constant heat flux. Liquid enters at T_{sat} with a fully-developed laminar velocity profile, as indicated by the velocity colour map used for the adiabatic section. On the heated wall, a superheated thermal boundary layer ($T > T_{sat}$) develops, as indicated by the temperature colour map used for the heated section.

When $\epsilon \to \infty$, so increasingly flatter channels are considered, the channel height converges to the asymptotic value of $D_h/2$, while the width increases indefinitely. This will have an impact on the film thickness and heat transfer trends with increasing ϵ, as will be shown later on. The pressure and velocity boundary conditions are the same as those indicated in Section 3.1. At the channel inlet, liquid enters at saturated conditions $T = T_{sat}$; a zero-gradient temperature condition is fixed at the outlet. A preliminary liquid-only single-phase simulation is run to obtain steady-state velocity and temperature fields, to be used as initial fields for the two-phase flow simulation, see Fig. 3. The two-phase simulations start with an initial vapour bubble placed upstream

of the channel, centred along the $z-$axis. The volume of this initial bubble is the same for all the values of ϵ, and it corresponds to an equivalent diameter of $1.63D_h$. Bubble nucleation at the wall is not included in the present numerical model and therefore only one bubble flows through the channel.

For each value of the channel aspect-ratio investigated, three simulations are performed by varying the capillary number of the liquid flow, $\mathrm{Ca_l} = \mu_l U_l/\sigma$, in the range $\mathrm{Ca_l} = 0.005 - 0.05$, and maintaining a constant value of the liquid Reynolds number, $\mathrm{Re_l} = \rho_l U_l D_h/\mu_l = 100$. The chosen values of $\mathrm{Ca_l}$ and $\mathrm{Re_l}$ represent well the flow of water or refrigerant fluids (R245fa, R134a, HFE7000, etc.) within channels of $D_h = 0.1 - 1\,\mathrm{mm}$, and mass fluxes of $G = 200 - 2000\,\mathrm{kg/(m^2 s)}$, which are common for microchannel flow boiling. The Reynolds number has a minor impact on the liquid film thickness [45], and therefore varying $\mathrm{Ca_l}$ while keeping a constant $\mathrm{Re_l}$ enables us to isolate the impact of the liquid film topology on the heat transfer, while the effect of single-phase heat convection remains constant. The Prandtl number of liquid and vapour, $\mathrm{Pr} = \mu \mathrm{c_p}/\lambda$, and the liquid to vapour density, viscosity, specific heat and thermal conductivity ratios, are all set to correspond to the fluid R245fa at $T_{sat} = 31\,^{\circ}\mathrm{C}$; see Tab. 1. The boiling number of the flow, $\mathrm{Bl} = q/(\rho_l U_l h_{lv})$, is fixed to $\mathrm{Bl} = 10^{-4}$ which, for the fluids and conditions specified above, corresponds to a heat flux on the order of $q = 10\,\mathrm{kW/m^2}$. A summary of the operating conditions simulated is reported in Tab. 1.

Within the range of conditions simulated, the Bond number of the flow $\mathrm{Bo} = \rho_l g R_h^2/\sigma \ll 1$, with g being the acceleration of gravity at terrestrial level, which justifies the approximation of negligible gravitational forces. Van der Waals forces at the channel walls are not included, and therefore film dry-

Table 1: Summary of the operating conditions investigated in the present study; three values of the liquid capillary number are tested, $\mathrm{Ca_l} = 0.005, 0.01, 0.05$; for each $\mathrm{Ca_l}$, 12 different channel aspect ratios are simulated, $\epsilon = 1, 1.25, 1.5, 1.75, 2, 2.5, 3, 3.5, 4, 5, 6, 8$, for a total of 36 simulation runs. The remaining flow parameters are constant throughout the study.

$\mathrm{Ca_l}$	ϵ	$\mathrm{Re_l}$	Bl	$\mathrm{Pr_l}$	$\mathrm{Pr_v}$	ρ_l/ρ_v	μ_l/μ_v	$c_{p,l}/c_{p,v}$	λ_l/λ_v
$0.005 - 0.05$	$1 - 8$	100	10^{-4}	5.75	0.675	126	36	1.46	6.3

out occurs only if the film is completely depleted by the evaporation process. In real applications, a liquid film of thickness on the order of $1\,\mu$m and below may rupture due to van der Waals forces, depending on the wettability of the wall, fluid properties and surface roughness [46]. In this work, we reach thicknesses of $\delta/R_h \approx 0.01$, and therefore intermolecular forces should have a minor impact as long as $D_h \geq 0.2\,$mm. Thermocapillary effects related to surface tension gradients are not considered. Mazouchi and Homsy [47] demonstrated theoretically that a streamwise temperature gradient along the channel induces an axial motion of long bubbles, characterised by a capillary number $\mathrm{Ca} \approx 185\,(\Delta\sigma/\sigma)^5$. In the present conditions, the bubble motion associated with thermocapillary effects has a capillary number of about 10^{-5} (with $\Delta\sigma$ estimated based on a ΔT of 5 K), which is orders of magnitude smaller than $\mathrm{Ca_l}$, thus suggesting that thermocapillary effects do not impact the streamwise bubble dynamics. The available theory is not sufficient to conclude about the impact of thermocapillary forces on the cross-sectional liquid film profile and future research may focus in this direction.

The domain is discretised with a structured mesh made of orthogonal

hexahedra, see the illustration in Fig. 4. The core of the channel is uniformly meshed, while in the near-wall region elements are gradually refined down to 50 times their initial thickness, as indicated in Tab. 2. This ensures that even the thinnest liquid film is always discretised with at least about 10 cells, so that the very steep velocity and temperature gradients are resolved accurately. This mesh has been chosen following a grid convergence test, where both finer and coarser grids were considered; the values of the heat transfer coefficient showed less than 5 % difference when employing a mesh twice as fine in all the directions, while no appreciable differences were observed in the liquid film thickness.

Simulations are run on HPC, typically employing ten 12-core nodes (infiniband interconnection; available RAM: 40 GB per node) for each case, adopting OpenFOAM's scotch domain decomposition. Each simulation requires between 2500 and 5000 CPU hours to complete.

Table 2: Details of the mesh utilised for the flow boiling simulations. The notation is explained in Fig. 4. Only a quarter of the channel cross-section is modelled and the domain size is $0.5W \times 0.5H \times 30D_h$. The hydraulic diameter D_h (and R_h) is constant, while H and W change depending on ϵ, as indicated in Eq. (7). The same mesh is utilised for all the $\epsilon \leq 4$ cases, with the cells sizes adjusted depending on H and W; for $\epsilon > 4$, the size of the elements along x is halved compared to the $\epsilon \leq 4$ configuration.

	Δ_x	Δ_y	Δ_z	$\Delta_{x,min}$	$\Delta_{y,min}$	Mesh size
$\epsilon \leq 4$	$0.012W$	$0.012H$	$0.048R_h$	$2.4 \cdot 10^{-4}W$	$2.4 \cdot 10^{-4}H$	$58 \times 58 \times 1266$
$\epsilon > 4$	$0.006W$	$0.012H$	$0.048R_h$	$1.2 \cdot 10^{-4}W$	$2.4 \cdot 10^{-4}H$	$116 \times 58 \times 1266$

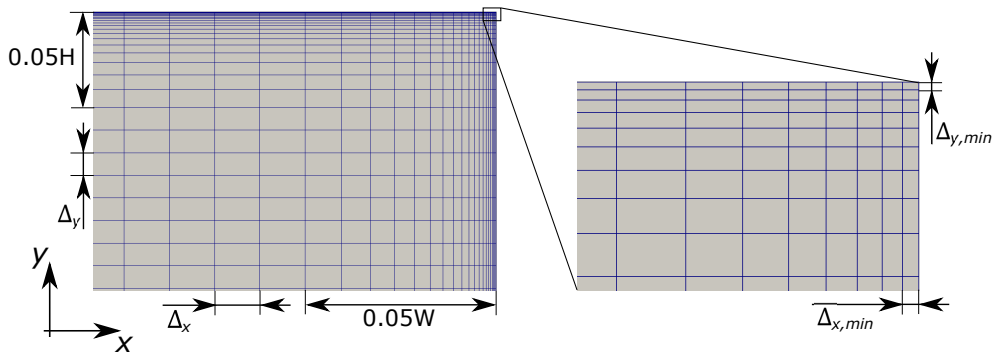

Figure 4: Illustration of the computational mesh (here $\epsilon = 2$) on a $x - y$ channel cross-section, near the top-right corner. Far from the wall, $x < 0.45W$ and $y < 0.45H$, cells have constant $\Delta_x \times \Delta_y \times \Delta_z$ size. Near the wall, $x > 0.45W$ and $y > 0.45H$, cells are gradually refined along x and y, down to minimum thicknesses $\Delta_{x,min}$ and $\Delta_{y,min}$. The values of cells thicknesses are reported in Tab. 2.

4.2. Bubble dynamics

At the onset of the flow, the liquid entering the channel transports the bubble downstream. When the liquid-vapour interface comes into contact with the superheated thermal boundary layer at the wall, evaporation begins. As liquid turns into vapour, the bubble nose accelerates downstream and the simulation terminates when the bubble nose reaches the outlet section. Figure 5 depicts the bubble profiles observed at different time instants on the horizontal symmetry plane ($y = 0$), for different aspect-ratios and $\mathrm{Ca_l} = 0.01$. Evaporation starts when the bubble nose reaches the axial location $z/D_h = 10$, which occurs after about $t/(R_h/U_l) = 10$ nondimensional time units; therefore, the darker blue profiles in Fig. 5 correspond to snapshots taken when evaporation has not yet occurred. For $\epsilon = 1$ and 2, the bubble is already elongated before entering in the heated section, and it quickly

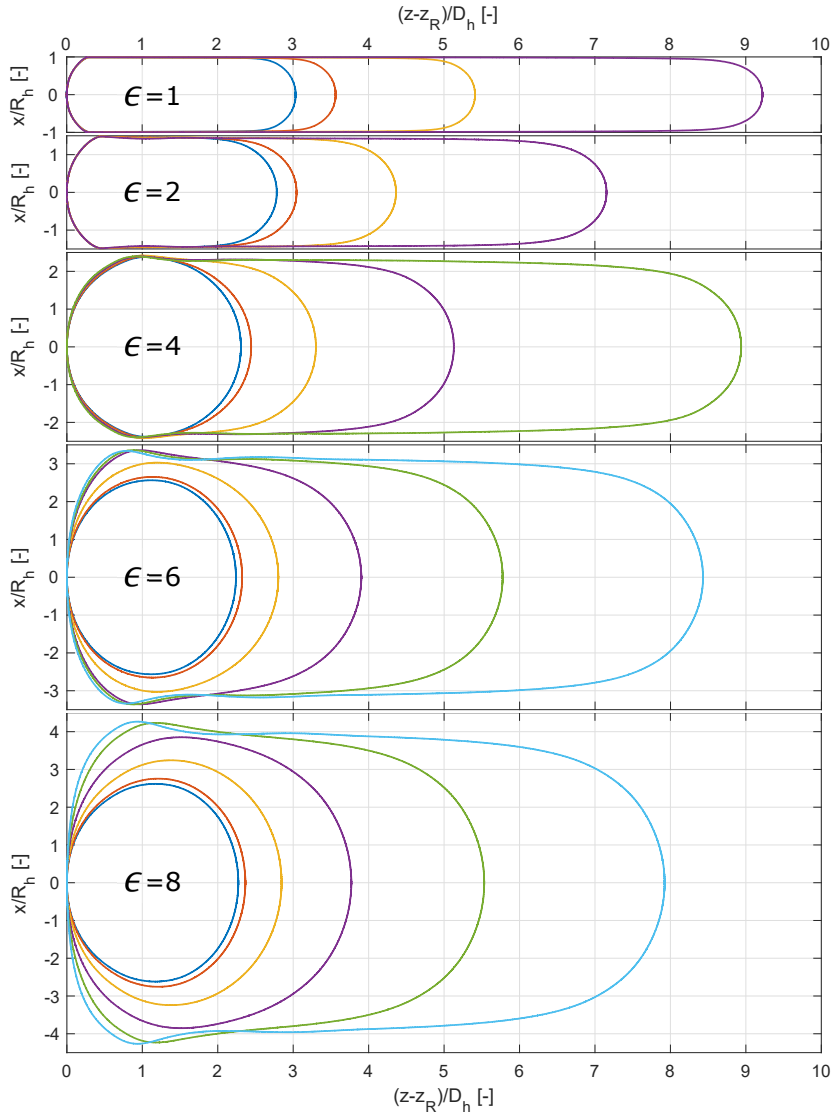

Figure 5: Bubble profiles for different channel cross-sections ($\mathrm{Ca_l} = 0.01$), observed on the $z - x$ plane ($y = 0$). The z coordinate is shifted to match the location of the bubble rear, z_R. The profiles are taken at the nondimensional time instants $t/(R_h/U_l) = 10$ (blue), 15 (red), 20 (yellow), 25 (purple), 30 (green), and 35 (cyan), with R_h/U_l being a time-scale.

grows in the downstream direction as evaporation begins. For $\epsilon \geq 4$, a bubble with the same initial volume exhibits little or no confinement along the width before entering in the heated section; therefore, the subsequent process of bubble growth proceeds first along the transversal direction, and then along the streamwise direction. Note that even after confinement, the elongated bubbles for $\epsilon \geq 4$ leave a thicker liquid film on the side wall of the channel compared to the smaller aspect-ratio cases, which is in line with the observations of de Lózar et al. [27, 28] for isothermal flows. Thicker films are more sensitive to inertial forces, since in thin-film flows inertia actually scales with the film thickness, rather than the size of the channel cross-section (i.e. D_h in this case) [48]. The increased inertial effects give rise to the undulations appearing near the tail of the long bubbles in Fig. 5, when larger ϵ are considered. The evolution of the bubble profiles for the other capillary numbers tested is analogous and is not reported here.

The velocity of the bubble nose and the bubble volume as the bubble advances within the microchannel are presented in Fig. 6, for $\mathrm{Ca_l} = 0.05$. Both bubble speed and volume exhibit a linear or weakly exponential trend with z_N, as already observed in the case of slug flow in circular channels [34]. For increasing values of the channel aspect-ratio, the velocity of the bubble nose decreases as indicated also by the profiles in Fig. 5, while the bubble volume increases. These trends can be explained by developing a simple energy balance. We consider a bubble of length L_b, which varies in time owing to liquid evaporation. We assume that the bubble occupies the entire cross-section of the channel, and thus has volume AL_b, while the surface area in contact with the channel wall is PL_b. If all the heat applied to the wall

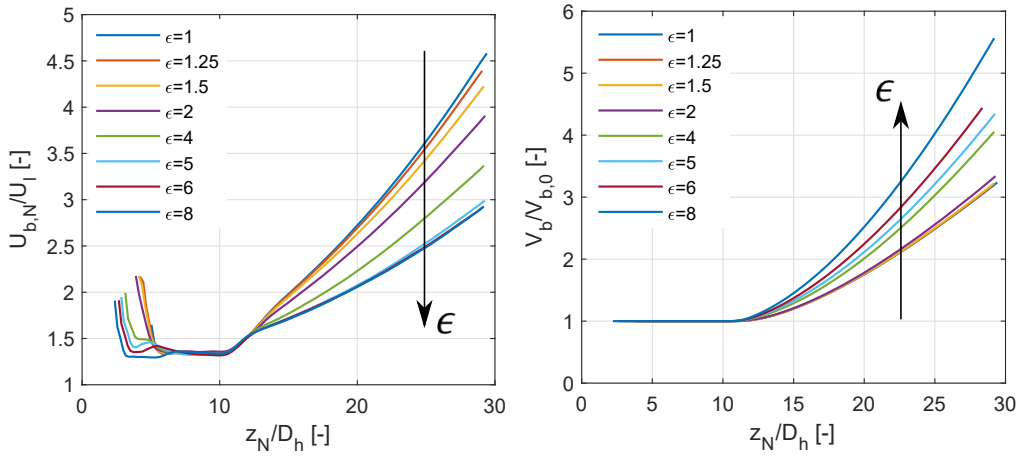

(a) (b)

Figure 6: (a) Nondimensional speed of the bubble nose and (b) bubble volume plotted as a function of the bubble nose position, z_N, for $\mathrm{Ca_l} = 0.05$. The bubble speed is rescaled by the average liquid velocity, U_l. The bubble volume is rescaled by its initial volume, $V_{b,0}$. The start of the heated region is at $z/D_h = 10$. The arrows indicate the direction of increasing channel aspect-ratio. Note that some of the curves overlap and therefore are not visible.

in contact with the bubble is converted into latent heat, the time-derivative of the bubble mass, $M_b = \rho_v A L_b$, can be estimated as:

$$\frac{d(\rho_v A L_b)}{dt} = \frac{qPL_b}{h_{lv}} \tag{8}$$

which can be rearranged as:

$$\frac{dL_b}{dt} = \Gamma L_b \tag{9}$$

where $\Gamma = 4q/(\rho_v h_{lv} D_h)$ and is independent of the channel aspect-ratio. Equation (9) has solution $L_b(t) = L_{b,0} e^{\Gamma t}$, where $L_{b,0}$ is the bubble length before evaporation begins. This expression can be used to estimate the location

of the bubble nose versus time:

$$z_N = z_R + L_b = U_{b,0}t + L_{b,0}e^{\Gamma t} \tag{10}$$

where $z_R = U_{b,0}t$ as the bubble rear moves as the adiabatic speed of the bubble, $U_{b,0}$ [34]. In the equation above, $t = 0$ corresponds to the time instant when the entire bubble is within the heated section, which starts at $z = 0$. Equation (10) can be differentiated in time to yield the velocity of the bubble nose:

$$U_{b,N} = U_{b,0} + L_{b,0}\Gamma e^{\Gamma t} \tag{11}$$

and can be developed further by taking $\Gamma t \ll 1$, such that $U_{b,N} = U_{b,0} + L_{b,0}\Gamma(1+\Gamma t)$. This assumption is valid during the initial stage of boiling, when t is still small. We can now express the time t as a function of z_N by applying the same linearisation to Eq. (10), which yields $t = (z_N - L_{b,0})/(U_{b,0} + L_{b,0}\Gamma)$, and substitute this back into the linearised expression of $U_{b,N}$:

$$U_{b,N} = U_{b,0} + \frac{L_{b,0}\Gamma}{U_{b,0} + L_{b,0}\Gamma}(U_{b,0} + \Gamma z_N) \tag{12}$$

From the equation above, we can extract the slope of the $z_N - U_{b,N}$ curve:

$$\frac{dU_{b,N}}{dz_N} = \frac{L_{b,0}\Gamma^2}{U_{b,0} + L_{b,0}\Gamma} \tag{13}$$

Under the conditions simulated here, $U_{b,0} \gg L_{b,0}\Gamma$, and therefore Eq. (13) can be simplified to:

$$\frac{dU_{b,N}}{dz_N} = \frac{L_{b,0}\Gamma^2}{U_{b,0}} = \frac{V_{b,0}}{D_h^2}\frac{\epsilon}{(1+\epsilon^2)}\frac{\Gamma^2}{U_{b,0}} \tag{14}$$

where $L_{b,0}$ has been rewritten as $L_{b,0} = V_{b,0}/A$. Since in the present study $V_{b,0}$, D_h and Γ are constant and independent of ϵ, while $U_{b,0}$ is only weakly

dependent on ϵ, Eq. (14) suggests that the bubble velocity decreases as the aspect-ratio increases, in agreement with the trend of Fig. 6(a).

From the same analysis it follows that the bubble volume along the channel can be expressed as:

$$V_b = \frac{V_{b,0}}{U_{b,0} + L_{b,0}\Gamma}(U_{b,0} + \Gamma z_N) \tag{15}$$

from which we extract the slope of the $z_N - V_b$ curve:

$$\frac{dV_b}{dz_N} = \frac{\Gamma}{U_{b,0} + L_{b,0}\Gamma} \tag{16}$$

which increases as larger aspect-ratios are considered due to the decrease of $L_{b,0}$, thus confirming the trend observed in Fig. 6(b).

For $\mathrm{Ca_l} = 0.005$ and 0.01, the bubble speed and volume follow the same behaviour versus the channel aspect-ratio as observed in Fig. 6. Furthermore, the bubble velocity decreases slightly when reducing the liquid capillary number, because $U_{b,0}/U_l$ also reduces. Conversely, the bubble volume increases for smaller $\mathrm{Ca_l}$, because it takes more time for the bubble to travel across the heated section.

4.3. Liquid film distribution

We analyse the distribution of the liquid film around the bubble by considering a cross-section located half-way between the bubble nose and rear tips, $z = (z_N + z_R)/2$, at a time-instant where the bubble approaches the channel end. The bubble profiles for different aspect-ratios and capillary numbers are depicted in Fig. 7. As a general trend, the area of the bubble cross-section reduces when the capillary number increases as viscous forces overcome capillary forces. The bubble profiles always exhibit a dimple along the longer

wall for $\epsilon \geq 2$, while for $\epsilon \leq 1.5$ no dimple is observed at $\mathrm{Ca_l} = 0.05$. Higher aspect-ratio channels promote the formation of an extended liquid film region on the longer wall, while a very thick film is left along the shorter wall, which results in a larger liquid fraction at the corners. de Lózar et al. [28] reported that the liquid area fraction on the cross-section increased mono-

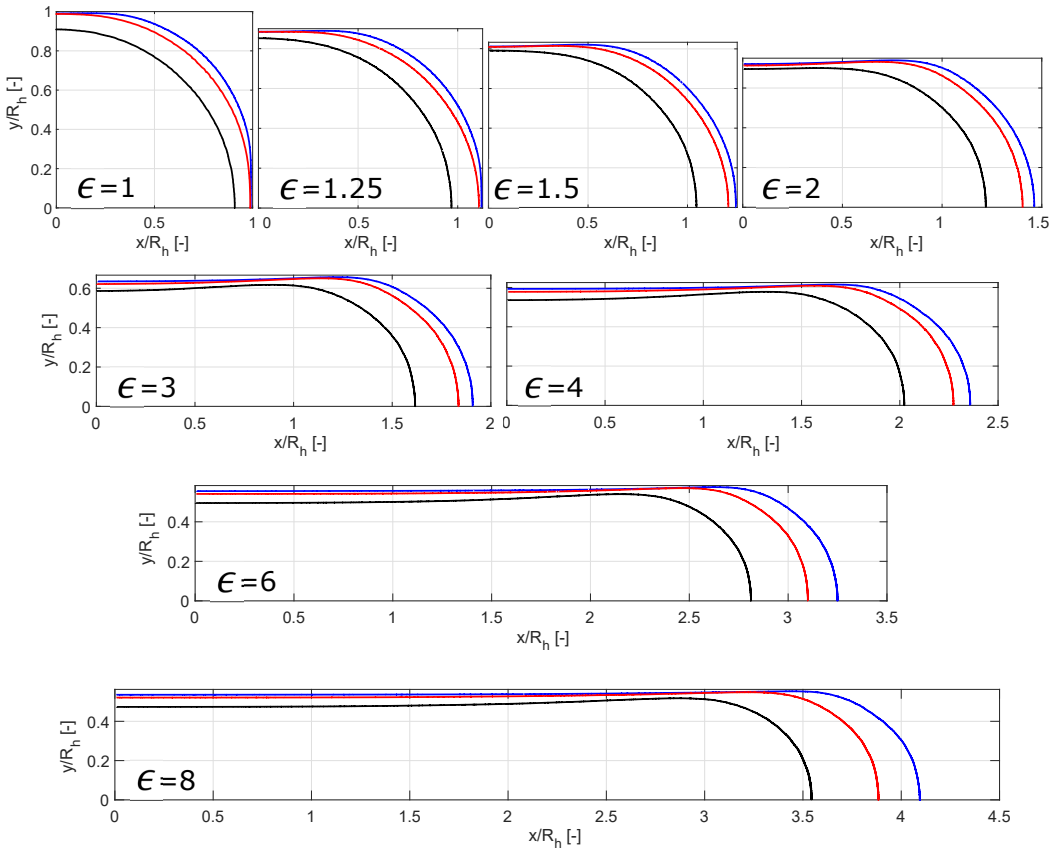

Figure 7: Interface profiles on a cross-section ($x - y$ plane) located half-way along the bubble, $(z_N + z_R)/2$, extracted for a time instant when the bubble nose approaches the channel outlet ($z_N/D_h = 29.5$). Colour legend: blue $-$ $\mathrm{Ca_l} = 0.005$; red $-$ $\mathrm{Ca_l} = 0.01$; black $-$ $\mathrm{Ca_l} = 0.05$.

tonically with ϵ when $\mathrm{Ca_b} > 0.035$. In this regime, they showed that the liquid fraction curves versus $\mathrm{Ca_b}$ for different ϵ collapse onto a single curve when rescaling the capillary number as $\mathrm{Ca_b} f(\epsilon)$, with $f(\epsilon)$ increasing monotonically with ϵ ($f \geq 1$ for $\epsilon \geq 1$), as if a long bubble propagating in a rectangular channel effectively "sees" a larger capillary number than a bubble in a square channel. Under the conditions presently simulated, the heat flux applied at the wall and the length of the heated section are not sufficient to completely evaporate the liquid film and therefore the wall is always wet.

A quantitative analysis of the different features of the cross-sectional liquid film topology when varying $\mathrm{Ca_l}$ and ϵ is provided in Fig. 8. In order to compare the absolute values of the film thickness at different ϵ, the thicknesses are rescaled by the constant parameter R_h, rather than H or W. The thickness of the liquid film measured at the centre of the top wall ($x = 0$, see Fig. 1), $\delta_{c,y}$, is plotted in Fig. 8(a). For $\mathrm{Ca_l} = 0.005$ and 0.01, $\delta_{c,y}$ is smallest in square channels and the value measured in the simulation, $\delta_{c,y} \approx 0.01 R_h$, is in agreement with those obtained for isothermal flows, see Fig. 2(a). When the aspect-ratio is increased above 1, the film thickness at the centre of the top wall increases due to the presence of the dimple at the bubble interface. Eventually, $\delta_{c,y}$ reaches an asymptotic value as $\epsilon \geq 5$. This is due to the fact that the bubble velocities converge to a constant value as $\epsilon \to \infty$ (see Fig. 6(a)), while $H \to R_h$, so that $\delta_{c,y}/R_h$ tends to a constant value as well. For $\mathrm{Ca_l} = 0.05$, the bubble is axisymmetric when $\epsilon = 1$, and $\delta_{c,y}$ drops as ϵ is increased, until a dimple forms on the interface (see Fig. 7); then, $\delta_{c,y}$ increases up to an asymptotic value, as observed for the lower capillary numbers. Aussillous and Quéré [49] developed a theory to describe the liquid film

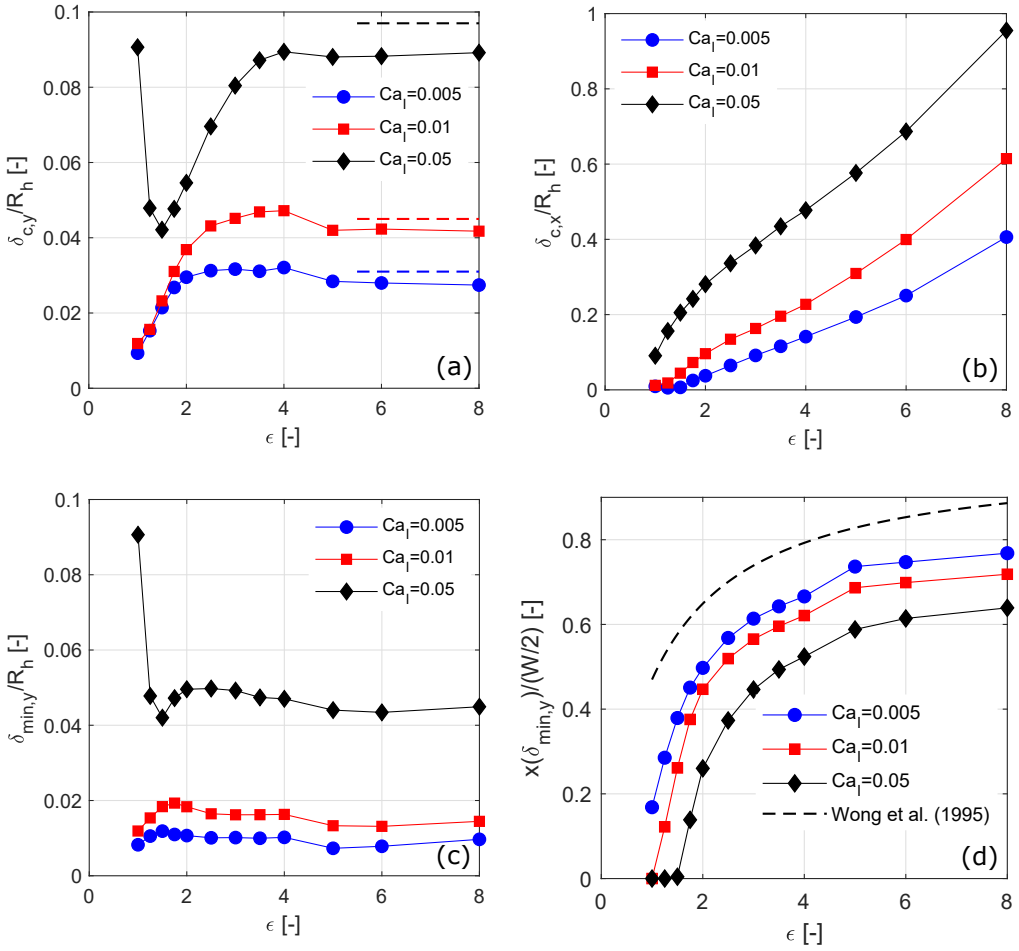

Figure 8: Liquid film thicknesses measured at the centre of the (a) top wall ($x = 0$) and (b) side wall ($y = 0$), (c) minimum film thickness detected on the top wall and (d) horizontal distance between the minimum thickness location and the centre of the top wall ($x = 0$); see Fig. 1 to identify the features plotted. In (a), the dashed lines indicate the predictions for $\epsilon \to \infty$ obtained using Eq. (17). In (d), the black dashed line corresponds to the prediction obtained by means of the asymptotic theory of Wong et al. [25] for $Ca_b \to 0$. Film thicknesses are measured on the same cross-section as described in Fig. 7.

around long bubbles travelling in two-dimensional channels, which led to the following relationship for the film thickness:

$$\frac{\delta}{\ell} = \frac{1.34\mathrm{Ca_b}^{2/3}}{1 + 3.35\mathrm{Ca_b}^{2/3}} \tag{17}$$

where ℓ is a characteristic length scale of the cross-section. Hence, Eq. (17) can be utilised to predict $\delta_{c,y}$ in rectangular channels in the asymptotic regime $\epsilon \to \infty$ (two-dimensional flow between parallel plates), by replacing ℓ with an appropriate length scale, here $H/2$ or $R_h/2$ (as $H \to R_h$). Introducing the values of $\mathrm{Ca_b}$ extracted from the simulations for $\mathrm{Ca_l} = 0.005$, 0.01, 0.05 and $\epsilon = 8$, respectively $\mathrm{Ca_b} = 0.0125$, 0.026, 0.15, in Eq. (17), yields the asymptotic film thicknesses $\delta_{c,y}/R_h = 0.031$, 0.045, 0.097, which are represented as dashed lines in Fig. 8(a) and compare very well with the simulation results.

The thickness of the liquid film measured at the centre of the side wall ($y = 0$), $\delta_{c,x}$, is plotted in Fig. 8(b). In general, $\delta_{c,x}$ increases monotonically with ϵ, except for $\mathrm{Ca_l} = 0.005$ and $\epsilon = 1 - 1.5$ where the disappearance of the interfacial dimple along the shorter wall (see Fig. 7) induces an opposite trend. We point out that the ratio $\delta_{c,x}/(W/2)$, not shown in the figure, exhibits an approximately linear trend with ϵ, as $\epsilon \to \infty$. This suggests that $\delta_{c,x}/R_h \sim \epsilon^2$ at larger aspect-ratios in Fig. 8(b), i.e. the film thickness measured on the side wall increases with ϵ at a faster rate than the channel width does [28].

The minimum film thickness measured from the top wall of the channel, $\delta_{min,y}$, is displayed in Fig. 8(c). Excluding the cases where the interface dimple is not formed, $\delta_{min,y}$ is approximately constant when varying ϵ. The slightly decreasing trend when $\epsilon > 2$ is ascribed to the decreasing velocity of the bubble, as suggested by Fig. 6(a). Notably, the minimum film thickness

can be $2-3$ times smaller than the thickness detected at the centre of the top wall. Figure 8(d) indicates the distance of this thinnest film region from the $x = 0$ axis. The figure includes also the prediction obtained using the asymptotic theory for a quasi-static meniscus proposed by Wong et al. [25], for the limiting case that $\mathrm{Ca_b} \to 0$. As higher aspect-ratio channels are considered, the minimum film thickness region moves towards the channel corners. This results in $60-80\,\%$ of the top wall being covered by a thin liquid film, which is expected to be beneficial for the heat transfer performance. For instance, Khodaparast et al. [24] utilised long bubbles to detach bacteria adhering to the walls of microchannels. For $\mathrm{Ca_b} = 10^{-3}$, the capillary forces generated by the liquid-gas interface were effective in removing $100\,\%$ of the bacteria in a region $x < 0.25W$ for $\epsilon = 1$, and $x < 0.4W$ for $\epsilon = 5$, while the efficiency dropped at the channel corners. Such a localised efficiency was attributed to the presence of a thin liquid film along the channel wall, and the extension of the clean-wall region measured in the experiment agrees remarkably with the numerical data in Fig. 8(d). It is worth noting that, due to the very thin films detected in correspondence of the interface dimple, liquid film dryout is likely to be triggered at the locations indicated in Fig. 8(d), and thus far from the centre of the channel walls, in agreement with the experimental observations of Khodaparast et al. [50] and Kreutzer et al. [51].

4.4. Heat transfer

In this section, we study the heat transfer performance induced by the transit of the long bubbles and the evaporation of the thin liquid film, by exploiting the understanding of the liquid film topology gained in the pre-

vious section. The temperature contours on a cross-section located half-way along the bubble, while it transits within the heated region, are displayed in Fig. 9 for $\epsilon = 1 - 4$ ($\mathrm{Ca_l} = 0.005$). It can be seen that the very thin liquid films formed around the bubbles are very effective in cooling down the channel wall. The highest temperatures are measured at the channel corners, which may become active nucleation sites at larger heat fluxes [9]. Since much thicker films are present along the shorter wall of the channel when $\epsilon > 1$, the heat transfer is considerably nonuniform around the channel perimeter in rectangular cross-sections. At $\epsilon = 4$, it can be seen in Fig. 9 that the superheated thermal boundary layer at the channel corners is convected towards the centre of the side wall. This effect is due to the transversal draining flows that drive liquid from the thin film region at the centre of the top (or bottom) wall towards the corners [26], thus forming a clockwise vortex (when observed on the $x \geq 0$ and $y \geq 0$ semi-plane). The pressure in the liquid region along the top wall is larger than the pressure within the bubble, while at the corners the liquid pressure is $\approx 2\sigma/H$ lower, and hence this transversal transport of fluid and heat becomes more effective as higher aspect-ratio channels are considered.

Figure 10 presents a comparative view of the local Nusselt number characterising heat transfer on the top wall of the channel and of the corresponding film thickness ($\epsilon = 1{-}4$, $\mathrm{Ca_l} = 0.005$). The Nusselt number is calculated from the heat transfer coefficient, $\mathrm{Nu} = hD_h/\lambda_l$, with $h = q/(T_w - T_{sat})$, and T_w being the wall temperature extracted from the simulations. As expected, the best heat transfer performances are observed where the liquid film is thinner; this corresponds to a narrow region along the channel centre in the square

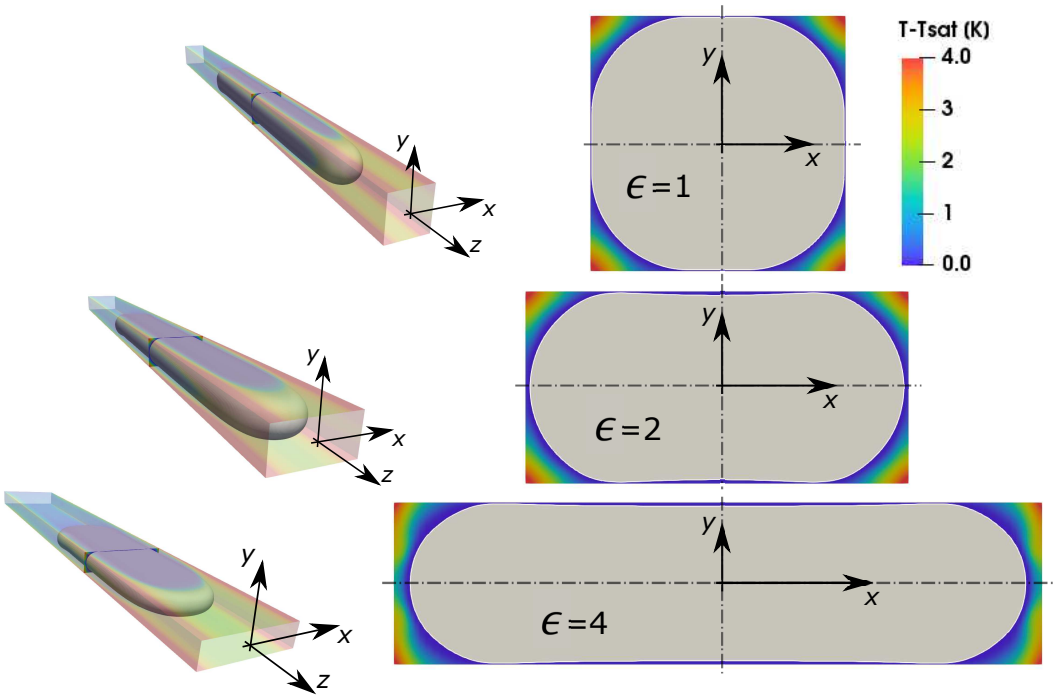

Figure 9: Contours of the temperature field extracted on a cross-section ($x-y$ plane) located half-way along the bubble, when it approaches the channel end, for $\mathrm{Ca_l} = 0.005$. The images on the left illustrate the bubble and the location of the cross-section under analysis; the channel wall is coloured by the temperature field. The same colour legend applies to all the temperature contours.

microchannel, while this region becomes more extended towards the corners as $\epsilon > 1$. The highest values of the Nusselt number are detected along the longitudinal lines where the liquid film is the thinnest, i.e. in correspondence to the interface dimple, see Fig. 8(d). The liquid film becomes thinner towards the rear of the bubbles at a rate $d\delta/dz$ that increases with ϵ. The rate of film depletion due to evaporation can be estimated as $d\delta/dz = \mathrm{Bl} = 10^{-4}$; this value is one order of magnitude smaller than the actual rate extracted

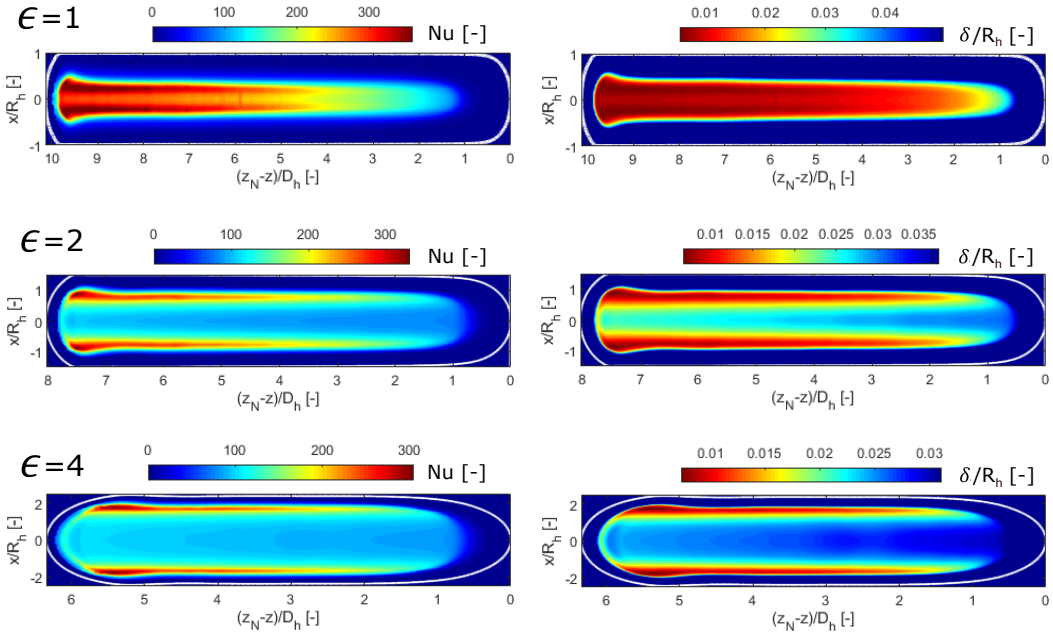

Figure 10: Contours of the Nusselt number and liquid film thickness measured on the top of the channel for different aspect-ratios and $\mathrm{Ca_l} = 0.005$. Within each box, the white line indicates the bubble profile on the $z - x$ plane ($y = 0$). Figures not to scale.

from the simulations, and hence the longitudinal thinning of the liquid film observed in Fig. 10 can be ascribed to the transversal draining flows.

A more quantitative analysis of the interplay between liquid film topology and heat transfer is provided in Figs. 11 ($\mathrm{Ca_l} = 0.005$) and 12 ($\mathrm{Ca_l} = 0.05$), where the local Nusselt number and liquid film thickness on the top and side walls of the channel, extracted on a cross-section located half-way along the bubble, are plotted for different aspect-ratios. For $\mathrm{Ca_l} = 0.005$, all the bubble profiles exhibit the interfacial dimple along the top wall (see also Fig. 7). A very high Nusselt number is measured for the square channel,

where a very thin film occurs, while high peaks of Nu are identified for $\epsilon \geq 5$ as well due to a decrease of the bubble velocity, which makes the film slightly thinner than the cases where $1 < \epsilon < 5$. We remark that the existence and stability of such thin films in a real case would depend on their absolute thickness. As the aspect-ratio of the channel increases, the portion of the

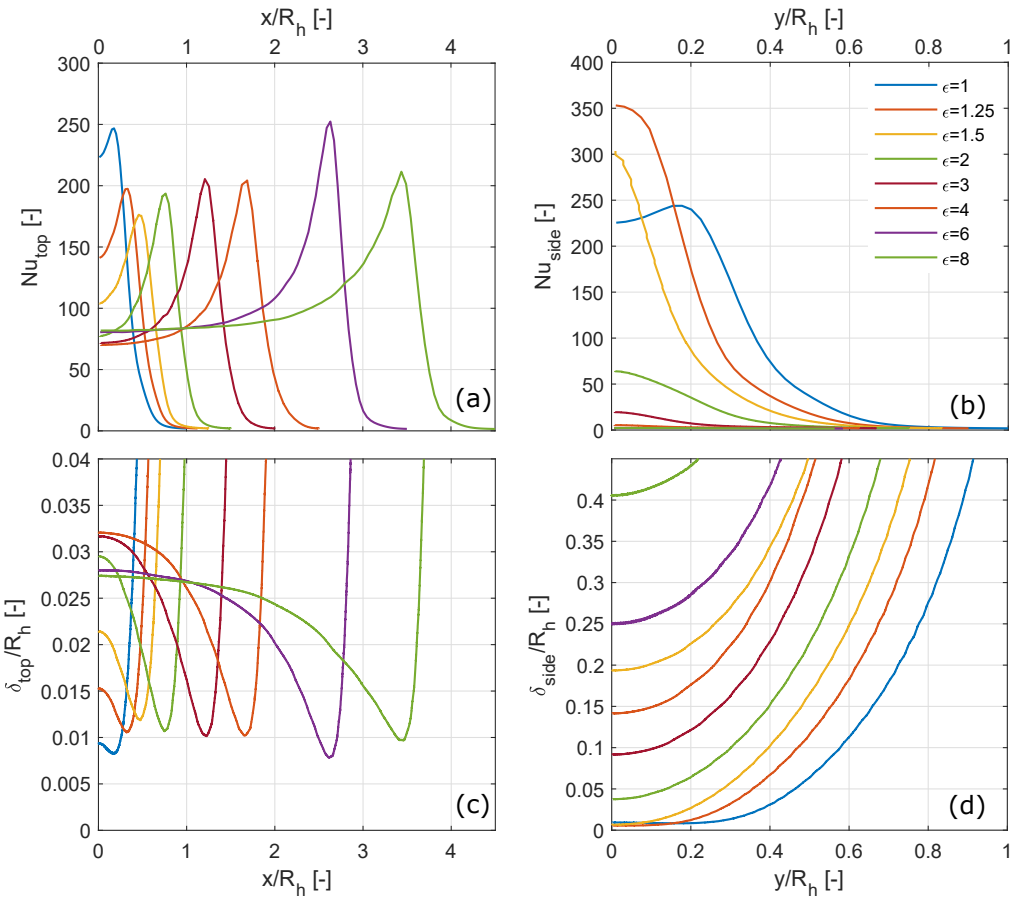

Figure 11: Local Nusselt number and liquid film thickness for $\mathrm{Ca_l} = 0.005$, measured on the same cross-section as described in Fig. 7; (a) and (c) are measured on the top wall, (b) and (d) on the side wall.

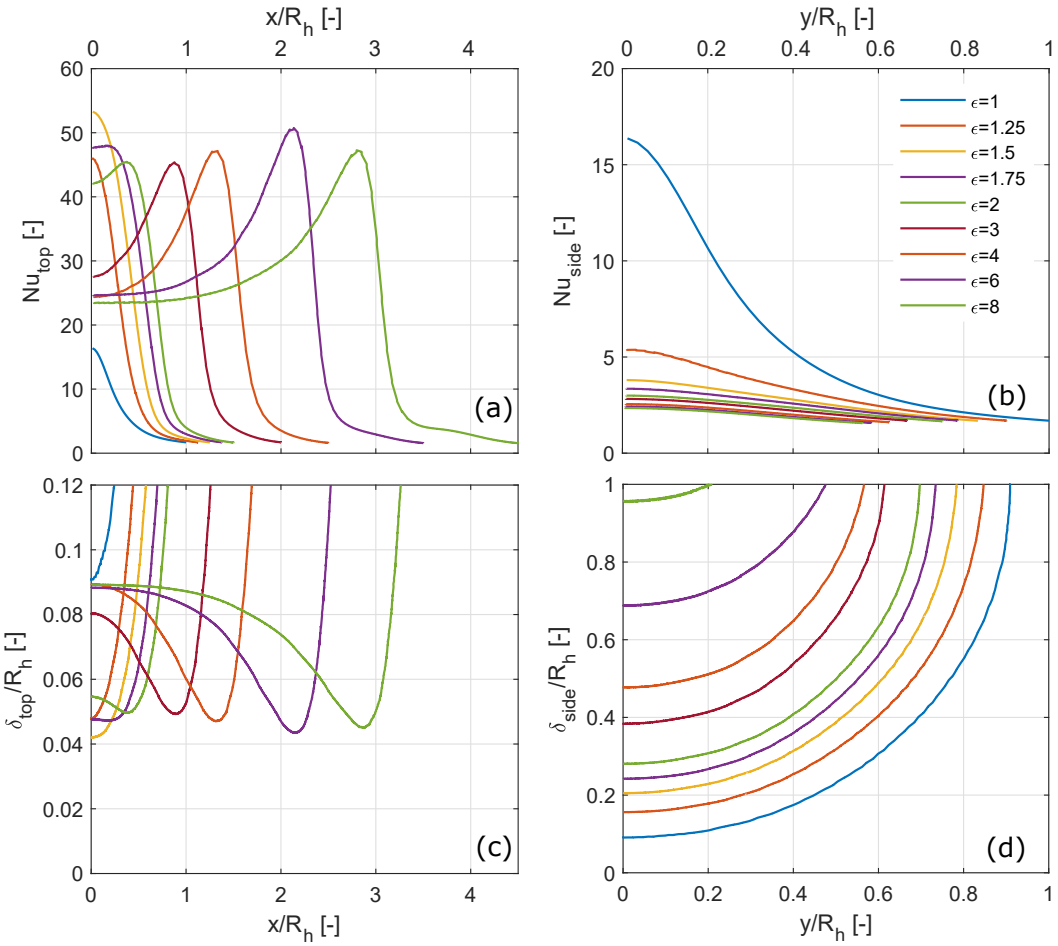

Figure 12: Local Nusselt number and liquid film thickness for $Ca_l = 0.05$, measured on the same cross-section as described in Fig. 7; (a) and (c) are measured on the top wall, (b) and (d) on the side wall.

top wall covered by the thin film, and therefore subject to very efficient heat transfer, becomes wider. On the shorter side of the microchannel, Fig. 11(b) and 11(d), the highest Nu is measured at the wall centre for $\epsilon = 1.25$, as the liquid film is the thinnest; the Nusselt number drops considerably as wider

channels are considered due to the larger amount of liquid left along the side wall. In general, very large values of Nu are achieved in correspondence to the locations of the very thin liquid films. This hints at steady-state heat conduction governing heat transfer across the thin film, which yields $h \approx \lambda_l/\delta$, and hence $\mathrm{Nu} \approx 2R_h/\delta$. In the data presented in Fig. 11, there is a perfect correspondence between the Nusselt number back-calculated from the film thickness and that calculated from the wall temperature, as long as the film is sufficiently thin.

For $\mathrm{Ca_l} = 0.05$, much smaller magnitudes of the heat transfer coefficient are observed, see Fig. 12, due to substantially thicker liquid films. The poorest heat transfer performances along the top wall are detected when the square channel is employed, due to the axisymmetric shape of the bubble and therefore thicker liquid film (see also Fig. 8(a)). The Nusselt number increases as ϵ is increased and reaches a local maximum when $\epsilon = 1.5$ owing to the film profile, while at larger aspect-ratios the bubble interface along the top wall changes curvature, so that Nu slightly decreases while the peak of the heat transfer shifts sideways. Along the channel side, the heat transfer is very poor because the wall is covered by a thick volume of liquid, and we notice that, when $\epsilon > 1$, $\mathrm{Nu} < 2R_h/\delta$, which indicates that the heat transfer across the thick film has not yet achieved steady-state [34].

A summary of the heat transfer results obtained with the numerical simulations for different ϵ and $\mathrm{Ca_l}$ is presented in Fig. 13. The figure reports the average Nusselt number measured around the channel perimeter, along the region occupied by the bubble ($z_R < z < z_N$). For $\mathrm{Ca_l} = 0.005$, the best heat transfer is obtained with the square channel, due to the very thin

liquid film occurring at the centre of the channel, although this covers only about 20 % of the cross-section; Nu drops at intermediate values of ϵ as the film along the top wall thickens, then it rises again at larger aspect-ratios as a larger fraction of the channel perimeter is covered by the thin film (up to 80 % of the top wall), eventually reaching an asymptotic limit as $\epsilon \geq 5$. Note that, for larger heat fluxes than those applied here, the thin liquid film observed at the centre of the wall for $\epsilon = 1$ may quickly evaporate and dry out, with a consequent drop of heat transfer performance. Trends are similar for $\mathrm{Ca_l} = 0.01$, although the heat transfer deteriorates due to thicker liquid films. The Nusselt number at larger aspect-ratios catches up the high values measured for $\epsilon = 1$, because the transversal extension of the liquid film for $\epsilon = 1$ is considerably smaller (see also Fig. 8(d)) compared to the $\mathrm{Ca_l} = 0.005$ case. The situation is substantially different at the largest capillary number tested, $\mathrm{Ca_l} = 0.05$, where the square channel exhibits the lowest average Nusselt number due to the disappearance of the thin-film region. In such conditions, the extended film region promoted by larger aspect-ratio channels benefits heat transfer greatly, and Nu increases monotonically with ϵ, till asymptotic conditions are achieved. In general, rectangular channels exhibit a strongly nonuniform heat transfer distribution along the channel perimeter, with the Nusselt number being $1 - 2$ orders of magnitude smaller along the shorter side.

The values of the average Nusselt number reported in Fig. 13 can be made dimensional, thus enabling a comparison with data from the literature. Al-Zaidi et al. [52] performed flow boiling experiments using the fluid HFE7100 within a multi-microchannel evaporator with channels of $D_h = 0.46\,\mathrm{mm}$ and

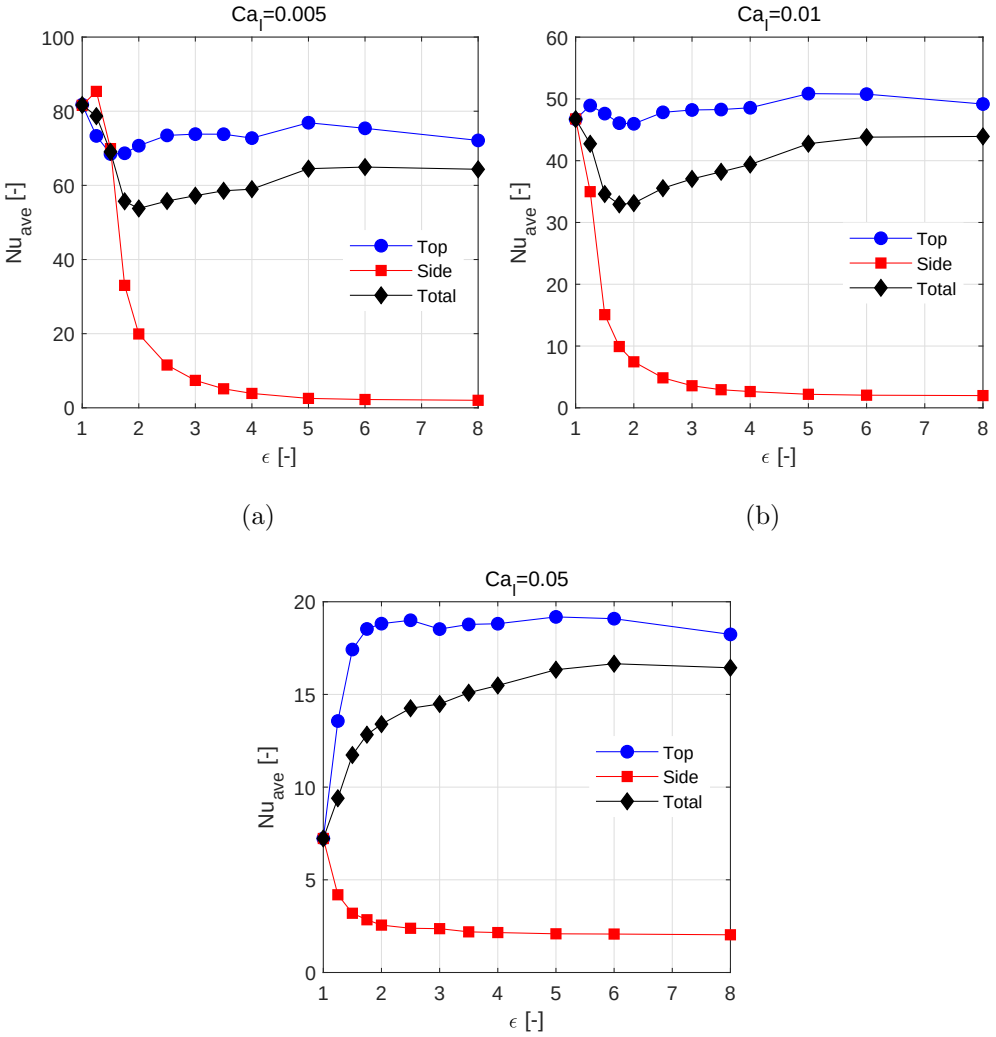

Figure 13: Average Nusselt number measured between z_R (bubble rear) and z_N (bubble nose), with $z_N/D_h = 29.5$.

aspect-ratio $\epsilon = 2$, heated from below. For a mass flux of $G = 250\,\mathrm{kg/(m^2 s)}$ (corresponding to $\mathrm{Ca_l} = \mu_l G/(\rho_l \sigma) = 0.004$) and heat flux in the range

$q = 26 - 68\,\mathrm{kW/m^2}$, they measured $h = 6 - 8\,\mathrm{kW/(m^2K)}$ at vapour qualities that can be attributed to slug flow. Using the numerical data in Fig. 13(a), $\mathrm{Nu} = 70$ on the top wall for $\epsilon = 2$, which yields $h = \mathrm{Nu}\lambda_l/D_h = 9\,\mathrm{kW/(m^2K)}$, in good agreement with the experiments. Fayyadh et al. [53] tested the refrigerant R134a within channels of $D_h = 0.42\,\mathrm{mm}$ and aspect-ratio $\epsilon = 0.43$, heated from below. For $G = 300\,\mathrm{kg/(m^2s)}$ ($\mathrm{Ca_l} = 0.006$) and low vapour qualities, they measured about $h = 5\,\mathrm{kW/(m^2K)}$. The mean Nusselt number along the side (shorter) wall for $\mathrm{Ca_l} = 0.005$ and $\epsilon = 2$ in Fig. 13(a) is $\mathrm{Nu} = 20$, which yields $h = 4\,\mathrm{kW/(m^2K)}$, thus matching the experiments quite well. Szczukiewicz et al. [54] studied boiling heat transfer of R236fa in square microchannels of $D_h = 0.1\,\mathrm{mm}$, and for $G = 1000\,\mathrm{kg/(m^2s)}$ ($\mathrm{Ca_l} = 0.02$) measured $h = 15 - 25\,\mathrm{kW/(m^2K)}$ at low vapour qualities. The numerical data in similar conditions, Fig. 13(b), suggest $\mathrm{Nu} = 47$ and $h = 35\,\mathrm{kW/(m^2K)}$; given the small channel diameter and high heat flux ($q = 170\,\mathrm{kW/m^2}$), film dryout is likely to occur in the experiment, thus motivating the larger heat transfer coefficient observed in the simulations. In summary, despite adopting an idealised fluid model, the magnitude of the heat transfer coefficient extracted from the simulations is in line with existing experimental data, which provides further validation to the numerical model.

5. Discussion

The results discussed in the previous section show that at lower capillary number, i.e. lower flow rates, the square channel exhibits the highest average Nusselt number. However, depending on the absolute size of the

channel, wall wettability and surface roughness, the very thin liquid film may rupture or dry out, with part of the wall becoming covered with vapour, and a consequent drop of the heat transfer performance. In such case, the heat transfer penalty of using larger channel aspect-ratios may be counter-balanced by a smaller extension of the dry area, as the latter would be limited to only a little region around the dimple. At higher capillary numbers, i.e. higher flow rates, the Nusselt number is larger for higher aspect-ratio cross-sections, while square channels perform very poorly. The heat transfer along the shorter wall is significantly smaller than that along the longer wall, and this may have important implications in two-phase cooling applications, where the heat load is not uniformly distributed around the microchannel perimeter. In a multi-channel evaporator, if the fin efficiency associated to heat transfer through the walls between the parallel channels is high (e.g. above 0.95 in Szczukiewicz et al. [55]), the microchannels should have the longer side orthogonal to the surface to be refrigerated, in order to increase the surface area of the fins and fit more channels per footprint area. For low fin efficiency, the evaporator should be designed with microchannels having the longer side in contact with the surface to be refrigerated.

The present results were obtained for relatively low heat flux conditions, which makes the heat transfer coefficient almost independent of the heat load (as, essentially, $h \approx \lambda_l/\delta$), while no liquid film dryout occurs. For larger heat fluxes or longer heated sections, the very thin films observed here may actually dry at the tail of the very long bubbles generated; in such cases, it is important to account for the impact of film evaporation (i.e. the heat load) on the longitudinal evolution of the film thickness. The best overall

heat transfer performance would result from the channel design that yields the best compromise between thin liquid films and limited extension of dry vapour regions.

We can exploit the understanding gleaned with the analysis of the interplay between liquid film distribution and heat transfer, to interpret the experimental observations reported in some studies from the literature. In the data of Soupremanien et al. [12], the channel was heated from the bottom and the heat transfer coefficient increased as ϵ was increased from $\epsilon = 2.3$ to 7, in agreement with the results of Fig. 13 (irrespective of $\mathrm{Ca_l}$). Fu et al. [14] investigated microchannels with $\epsilon < 1$ ($D_h = 1.12\,\mathrm{mm}$) heated from the bottom and the heat transfer coefficient decreased as the channels became narrower. Our numerical results suggest that this can be explained by the thickening of the liquid film in contact with the shorter wall (Fig. 8(b)). However, the progressive dryout of this film as ϵ decreased below 1 (as skecthed by the authors) is another potential explanation, owing to the very low mass fluxes employed ($\mathrm{Ca_l} < 10^{-3}$), but the theory of Wong et al. [25] suggests that the dry region along the shorter wall should become narrower as the channel flattens. Markal et al. [16] observed a sharp drop of the heat transfer as the aspect-ratio decreased from $\epsilon = 2.71$ to 1.22 in a small microchannel, $D_h = 0.1\,\mathrm{mm}$, and small capillary number, $\mathrm{Ca_l} = 0.003$. This can be ascribed to the quick evaporation and dryout of the very thin liquid film at the centre of the square channel, since $q > 70\,\mathrm{kW/m^2}$. Similarly, Al-Zaidi et al. [17] measured better heat transfer coefficients when $\epsilon > 1$, with $\mathrm{Ca_l} = 0.007$, which can be related to a reduction of the extension of the dry vapour region on the bottom wall of the channel.

6. Conclusions

This article presented a numerical study of the impact of the channel shape on boiling heat transfer in microchannels, using interface-resolved simulations. The numerical method is based on the VOF two-phase flow solver in OpenFOAM, here augmented by implementing a phase-change model that computes the rate of interfacial mass transfer according to the Hertz-Knudsen-Schrage relationship. We adopted a benchmark flow model where a single isolated bubble is seeded at the channel upstream, and transported by a liquid flow across the diabatic section, which is heated by a constant and uniform heat flux. We studied a range of flow conditions that apply well to the flow boiling of water or refrigerant fluids in sub-millimetre channels at low heat flux ($q \sim 10\,\mathrm{kW/m^2}$), and cross-sectional aspect-ratios $\epsilon = 1 - 8$, keeping the hydraulic diameter constant. The model predictions for the bubble velocity and liquid film thickness in noncircular channels were first validated against existing numerical results obtained for isothermal flow conditions. The numerical framework allows us to investigate in detail the impact of the channel shape on the topology and perimetral distribution of the liquid film and heat transfer, thus providing valuable suggestions for the design of multi-microchannel evaporators and future research directions:

- Bubbles growing in higher aspect-ratio channels need to travel further downstream to occupy the entire cross-section, and then leave a thin liquid film at the walls.

- Square microchannels exhibit a very thin liquid film region along the centre of the wall ($\delta/R_h \leq 0.01$) at low capillary numbers ($\mathrm{Ca_l} = 0.005$);

however, this thickness varies by one order of magnitude as the liquid flow rate is increased and the bubble cross-sectional shape becomes axisymmetric.

- Rectangular channels exhibit thicker liquid films as the aspect-ratio of the cross-section is increased, up to an asymptotic thickness reached when $\epsilon \geq 5$; however, this liquid film covers up to 80 % of the cross-section perimeter as the channel becomes flatter.

- At small capillary numbers, all the bubble profiles exhibit a dimple between the corners and the centre of the longer wall, and film dryout is likely to initiate where the film thickness has a minimum.

- The local heat transfer performances are strongly correlated to the local film thickness, as heat conduction dominates the wall-fluid heat transfer. The highest values of the Nusselt number are achieved where the film is the thinnest, i.e. at the liquid-vapour interface dimple, while it drops by orders of magnitude at the channel corners, where the liquid accumulates.

- At small capillary numbers, the square channel yields the best heat transfer performance, although the very thin film at the channel centre is more at risk of dryout.

- For increasing capillary numbers, the Nusselt number drops when $\epsilon = 1$ due to the disappearance of the thin film region, while higher aspect-ratio channels exhibit the best heat transfer performance, as they promote the formation of an extended liquid film covering the longer wall.

Asymptotic values of the Nusselt number are achieved when $\epsilon \geq 5$.

- As the aspect-ratio is increased, the average Nusselt number along the shorter wall becomes orders of magnitude smaller than the value obtained along the longer wall, due to a strong asymmetry in the liquid film perimetral distribution.

Acknowledgement

O. K. M. acknowledges funding from PETRONAS and the Royal Academy of Engineering for Research Chair.

References

[1] B. Agostini, M. Fabbri, J. E. Park, L. Wojtan, J. R. Thome, B. Michel, State of the art of high heat flux cooling technologies, Heat Transfer Eng. 28 (2007) 258–281.

[2] M. Gómez Marzoa, G. Ribatski, J. R. Thome, Experimental flow boiling heat transfer in a small polyimide channel, Appl. Therm. Eng. 103 (2016) 1324 – 1338.

[3] M. A. Safi, N. I. Prasianakis, J. Mantzaras, A. Lamibrac, F. B. Büchi, Experimental and pore-level numerical investigation of water evaporation in gas diffusion layers of polymer electrolyte fuel cells, Int. J. Heat Mass Tran. 115 (2017) 238 – 249.

[4] N. Lamaison, C. L. Ong, J. B. Marcinichen, J. R. Thome, Two-phase mini-thermosyphon electronics cooling: Dynamic modeling, experimen-

tal validation and application to 2U servers, Appl. Therm. Eng. 110 (2017) 481 – 494.

[5] I. Mudawar, Two-phase microchannel heat sinks: Theory, applications, and limitations, J. Electron. Packaging 133 (2011) 041002.

[6] T. G. Karayiannis, M. M. Mahmoud, Flow boiling in microchannels: Fundamentals and applications, Appl. Therm. Eng. 115 (2017) 1372 – 1397.

[7] L. Cheng, G. Xia, Fundamental issues, mechanisms and models of flow boiling heat transfer in microscale channels, Int. J. Heat Mass Tran. 108 (2017) 97 – 127.

[8] J. Lee, I. Mudawar, Critical heat flux for subcooled flow boiling in micro-channel heat sinks, Int. J. Heat Mass Tran. 52 (2009) 3341 – 3352.

[9] T.-H. Yen, M. Shoji, F. Takemura, Y. Suzuki, N. Kasagi, Visualization of convecting boiling heat transfer in single microchannels with different shaped cross-sections, Int. J. Heat Mass Tran. 49 (2006) 3884–3894.

[10] T. Harirchian, S. V. Garimella, Microchannel size effects on local flow boiling heat transfer to a dielectric fluid, Int. J. Heat Mass Tran. 51 (2008) 3724 – 3735.

[11] T. Harirchian, S. V. Garimella, The critical role of channel cross-sectional area in microchannel flow boiling heat transfer, Int. J. Multiph. Flow 35 (2009) 904 – 913.

[12] U. Soupremanien, S. Le Person, M. Favre-Marinet, Y. Bultel, Influence of the aspect ratio on boiling flows in rectangular mini-channels, Exp. Therm. Fluid. Sci. 35 (2011) 797–809.

[13] Y. Wang, K. Sefiane, Effects of heat flux, vapour quality, channel hydraulic diameter on flow boiling heat transfer in variable aspect ratio micro-channels using transparent heating, Int. J. Heat Mass Tran. 55 (2012) 2235–2243.

[14] B.-R. Fu, C.-Y. Lee, C. Pan, The effect of aspect ratio on flow boiling heat transfer of HFE-7100 in a microchannel heat sink, Int. J. Heat Mass Tran. 58 (2013) 53–61.

[15] C. W. Choi, D. I. Yu, M. H. Kim, Adiabatic two-phase flow in rectangular microchannels with different aspect ratios: Part I - Flow pattern, pressure drop and void fraction, Int. J. Heat Mass Tran. 54 (2011) 616 – 624.

[16] B. Markal, O. Aydin, M. Avci, Effect of aspect ratio on saturated flow boiling in microchannels, Int. J. Heat Mass Tran. 93 (2016) 130–143.

[17] A. H. Al-Zaidi, M. M. Mahmoud, T. G. Karayiannis, Flow boiling of HFE-7100 in multi-microchannels: aspect-ratio effects, in: 6th Micro and Nano Flows Conference, Atlanta, USA, 2018.

[18] J. R. Thome, V. Dupont, A. M. Jabobi, Heat transfer model for evaporation in microchannels. Part I: Presentation of the model, Int. J. Heat Mass Tran. 47 (2004) 3375–3385.

[19] M. Magnini, J. R. Thome, A CFD study of the parameters influencing heat transfer in microchannel slug flow boiling, Int. J. Therm. Sci. 110 (2016) 119–136.

[20] S. R. Rao, Y. Peles, Spatiotemporally resolved heat transfer measurements for flow boiling in microchannels, Int. J. Heat Mass Tran. 89 (2015) 482–493.

[21] Y. Han, N. Shikazono, N. Kasagi, The effect of liquid film evaporation on flow boiling heat transfer in a microtube, Int. J. Heat Mass Tran. 55 (2012) 547–555.

[22] Q. Zhang, S. M. Hassanizadeh, B. Liu, J. F. Schijven, N. K. Karadimitriou, Effect of hydrophobicity on colloid transport during two-phase flow in a micromodel, Water Resour. Res. 50 (2014) 7677–7691.

[23] Y. Hu, S. Bian, J. Grotberg, M. Filoche, J. White, S. Takayama, J. B. Grotberg, A microfluidic model to study fluid dynamics of mucus plug rupture in small lung airways, Biomicrofluidics 9 (2015) 044119.

[24] S. Khodaparast, M. K. Kim, J. Silpe, H. A. Stone, Bubble-driven detachment of bacteria from confined micro-geometries, Environ. Sci. Technol. 51 (2017) 1340–1347.

[25] H. Wong, C. J. Radke, S. Morris, The motion of long bubbles in polygonal capillaries. Part 1. Thin films, J. Fluid Mech. 292 (1995) 71–94.

[26] A. L. Hazel, M. Heil, The steady propagation of a semi-infinite bubble into a tube of elliptical or rectangular cross-section, J. Fluid Mech. 470 (2002) 91–114.

[27] A. de Lózar, A. L. Hazel, M. Heil, Scaling properties of coating flows in rectangular channels, Phys. Rev. Lett. 99 (2007) 234501.

[28] A. de Lózar, A. Juel, A. L. Hazel, The steady propagation of an air finger into a rectangular tube, J. Fluid Mech. 614 (2008) 173–195.

[29] C. W. Hirt, B. D. Nichols, Volume of fluid (VOF) method for the dynamics of free boundaries, J. Comput. Phys. 39 (1981) 201–225.

[30] A. Ferrari, M. Magnini, J. R. Thome, Numerical analysis of slug flow boiling in square microchannels, Int. J. Heat Mass Tran. 123 (2018) 928–944.

[31] J. U. Brackbill, D. B. Kothe, C. Zemach, A continuum method for modeling surface tension, J. Comput. Phys. 100 (1992) 335–354.

[32] V. P. Carey, Liquid-vapor phase change phenomena, Taylor and Francis, 1992.

[33] I. Tanasawa, Advances in condensation heat transfer, in: J. P. Hartnett, T. F. Irvine (Eds.), Advances in Heat Transfer, Academic Press, San Diego, 1991.

[34] M. Magnini, B. Pulvirenti, J. R. Thome, Numerical investigation of hydrodynamics and heat transfer of elongated bubbles during flow boiling in a microchannel, Int. J. Heat Mass Tran. 59 (2013) 451–471.

[35] S. Hardt, F. Wondra, Evaporation model for interfacial flows based on a continuum-field representation of the source terms, J. Comput. Phys. 227 (2008) 5871–5895.

[36] H. G. Weller, A new approach to VOF-based interface capturing methods for incompressible and compressible flows, OpenCFD Ltd. Report TR/HGW/04 (2008).

[37] B. van Leer, Towards the ultimate conservative difference scheme. V. A second-order sequel to Godunov's method, J. Comput. Phys. 32 (1979) 101–136.

[38] R. I. Issa, Solution of the implicitly discretized fluid flow equations by operator-splitting, J. Comput. Phys. 62 (1985) 40–65.

[39] C.-W. Kang, S. Quan, J. Lou, Numerical study of a Taylor bubble rising in stagnant liquids, Phys. Rev. E 81 (2010) 066308.

[40] F. P. Bretherton, The motion of long bubbles in tubes, J. Fluid Mech. 10 (1961) 166–188.

[41] L. E. Scriven, On the dynamics of phase growth, Chem. Eng. Sci. 10 (1959) 1–13.

[42] M. Magnini, J. R. Thome, Computational study of saturated flow boiling within a microchannel in the slug flow regime, J. Heat Transf. 138 (2016) 021502.

[43] L. Consolini, J. R. Thome, Micro-channel flow boiling heat transfer of R-134a, R-236fa, and R-245fa, Microfluid Nanofluid 6 (2009) 731–746.

[44] L. Consolini, J. R. Thome, A heat transfer model for evaporation of coalescing bubbles in microchannel flow, Int. J. Heat Fluid Flow 31 (2010) 115–125.

[45] M. T. Kreutzer, F. Kapteijn, J. A. Moulijn, C. R. Kleijn, J. J. Heiszwolf, Inertial and interfacial effects on pressure drop of Taylor flow in capillaries, AIChE J. 51 (2005) 2428–2440.

[46] G. F. Teletzke, H. T. Davis, L. E. Scriven, Wetting hydrodynamics, Rev. Phys. Appl. 23 (1988) 989–1007.

[47] A. Mazouchi, G. M. Homsy, Thermocapillary migration of long bubbles in cylindrical capillary tubes, Phys. Fluids 12 (2000) 542–549.

[48] M. Magnini, A. Ferrari, J. R. Thome, H. A. Stone, Undulations on the surface of elongated bubbles in confined gas-liquid flows, Phys. Rev. Fluids 2 (2017) 084001.

[49] P. Aussillous, D. Quéré, Quick deposition of a fluid on the wall of a tube, Phys. Fluids 12 (2000) 2367–2371.

[50] S. Khodaparast, O. Atasi, A. Deblais, B. Scheid, H. A. Stone, Dewetting of thin liquid films surrounding long bubbles in microchannels, Langmuir 34 (2018) 1363–1370.

[51] M. T. Kreutzer, M. S. Shah, P. Parthiban, S. A. Khan, Evolution of non-conformal Landau-Levich-Bretherton films of partially wetting liquids, Phys. Rev. Fluids 3 (2018) 014203.

[52] A. H. Al-Zaidi, M. M. Mahmoud, T. G. Karayiannis, Flow boiling of HFE-7100 in microchannels: Experimental study and comparison with correlations, Int. J. Heat Mass Tran. 140 (2019) 100–128.

[53] E. M. Fayyadh, M. M. Mahmoud, K. Sefiane, T. G. Karayiannis, Flow boiling heat transfer of R134a in multi microchannels, Int. J. Heat Mass Tran. 110 (2017) 422–436.

[54] S. Szczukiewicz, N. Borhani, J. R. Thome, Fine-resolution two-phase flow heat transfer coefficient measurements of refrigerants in multi-microchannel evaporators, Int. J. Heat Mass Tran. 67 (2013) 913–929.

[55] S. Szczukiewicz, N. Borhani, J. R. Thome, Two-phase heat transfer and high-speed visualization of refrigerant flows in $100 \,\mathrm{x}\, 100\,\mu\mathrm{m}^2$ silicon multi-microchannels, Int. J. of Refrigeration 36 (2013) 402–413.